INVESTIGATION OF NANOPARTICLES FOR USE IN MICROWAVE

SYSTEMS IN BIOMEDICINE

A Thesis

by

HOURA TAGHVAI

Submitted to the Office of Graduate Studies of
Texas A&M University
in partial fulfillment of the requirements for the degree of

MASTER OF SCIENCE

Chair of Committee,	Kenith Meissner
Committee Members,	Brian E. Applegate
	Sarah E. Bondos
Head of Department,	Gerald L. Cote

May 2013

Major Subject: Biomedical Engineering

ABSTRACT

This research focuses on the microwave properties of nanoparticles for use as contrast and hyperthermia agents. Currently, visible light is used for irradiation of nanoparticles as hyperthermia agents. Additionally, visible/Near-infrared light is used for photoacoustic tomography (PAT) imaging. Compared to optical wavelengths, frequencies in microwave range transmit through tissue with high penetration depth . Thus, deep cancerous cells and malignant tissue may be treated and imaged. These nanoparticles could enable the use of a hybrid microwave/acoustic technique known as thermoacoustic tomography.

Here, quantitative measurements of the heat generation in super paramagnetic iron oxide nanoparticle (SPIONs), gold nanoparticles (AuNPs), and gold nanoclusters (AuNCs) induced by microwave energy at 3 GHz, are presented and compared. Based on our experiments, SPIONs are the most efficient nanoparticles for microwave heating. Very high concentrations of SPIONs are able to convert microwave energy into heat about 22° C more than DI-water. AuNPs, which support plasmon resonances, do not provide heat under microwave irradiation as predicted by our computational analysis based on Mie Theory. AuNCs are a new form of ultra-small (<2.5 nm) AuNPs , which do not support plasmonic resonances and have supra-molecular properties such as sub-conduction band transitions. Interestingly, AuNCs have the potential to absorb microwave energy and may provide an alternative to SPIONs. These nanoparticles had not yet been studied before in this frequency region. In addition, the absorption coefficient of nanoparticles were calculated using complex permittivity data from a dip probe kit and a Vector Network Analyzer (VNA) in a broad band range from 500 MHZ to 10 GHz. This method allows identification of best frequency region with highest penetration depth. In the last step, the nanoparticles with different concentrations were tested as exogenous contrast agents in a Thermoacoustic Tomography (TAT) system. TAT utilizes the penetration depth of microwave energy while producing high resolution images through acoustic waves. The addition of an exogenous contrast agent improves

image quality by more effectively converting microwave energy to heat. The experiment reveals that the time resolved thermoacoustic signal (TA) from SPIONs is stronger than AuNPs and AuNCs and thus, the image contrast produced by SPIONs is stronger than the two other aforementioned nanoparticles.

DEDICATION

To My Parents

And

My Beloved Husband

TABLE OF CONTENTS

LIST OF FIGURES

CHAPTER I

INTRODUCTION AND RESEARCH BACKGROUND

1.1 Research Motivation

Medical imaging is used to create image for clinical purposes, or the study of human physiology. In the widest concept, medical imaging incorporates radiology, nuclear medicine, endoscopy, medical thermography, medical photography and microscopy. Biomedical engineering, medical physics, and computer science all contribute to the development of these techniques. Medical imaging techniques can be divided into invasive and noninvasive techniques. The term noninvasive is used for imaging modalities which do not penetrate the skin physically while invasive term is used to present technique which image the structures by making an opening the skin. In noninvasive case, medical imaging is achieved by the solution of mathematical inverse problem. This means that the properties of the living target is deduced from the effect (observed signal) [1]. On the other categorization, medical imaging is divided into ionizing and nonionizing techniques. The boundary which defines the ionizing and nonionizing is very fuzzy. In general, if the photon energy (in the case of electromagnetic radiation) of the radiation particle is greater than the ionization energy of the target, then each particle collision is able to ionize a target atom [2]. Of the 5 billion worldwide imaging investigations, two third of them are ionizing techniques [3].

An atom measures about 10^{-10} meters. The research of atoms and molecules is the conventional field of chemistry and was studied in late 19th century and 20th century. A nanometer (nm) or 10^{-9} m, includes collections of atoms and molecules. The study of bulk materials which includes micro scale particles or larger was the subject of solid state physics and material science. Nanoparticle materials were not studied by either group until the last decade of 19th century. It was shown that the properties of materials on the nanometer scale are dependent on their size and shape while bulk materials have

constant properties regardless of size. Size-dependent properties are observed, such as surface plasmon resonance in some metal nanoparticles and superparamagnetism in magnetic nanomaterials. These new properties are generated by the lack of interface symmetry or to electron confinement. Thus, nanometer-scale materials (1-100 nm) which are neither similar to the individual constitute nor the bulk materials. In other words, nanomaterials bridge the gap between bulk materials and atomic or molecular structures. On this scale, many atoms are at the surface of nanoparticles, or one layer removed from the surface. Since the properties are dependent on the size and shape of nanoparticles, properties can be changed within the same material just with varying the size and shape of nanoparticles. Nanomaterials research is currently an interesting and appealing area of research due to the wide variety of potential applications in biomedical, optical, and electronic fields. Taking advantage of the size-dependent properties and size similarity of nanoparticles with many biological components, we can use nanoparticles as very small probes to observe cellular machinery. Understanding biological processes on the nanoscale level is a strong driving force behind development of nanotechnology [4].

The nanometer scale is interesting in biological systems as many cellular components are 10s of nm in size. Artificial structures can be accurately engineered on the nanometer scale and can be incorporated into biological systems due to similar size scales. Biological systems are complex in terms of structure and function, although neither is well understood in detail. The ability to rationally design structures on the same size as biological molecules generates the ability to probe and modify biological systems [4].

Hyperthermia is a noninvasive approach to cancer treatment in which tissue is exposed to energy that, through the use of exogenous agents, causes higher localized temperature to promote selective destruction of abnormal cells. Many reports have shown that different portions of the spectrum can be used as the heat source in hyperthermia applications, including optical, radio and microwave frequencies [5-8]. Microwave

electromagnetic waves offer unique advantages over optical sources. Compared to optical wavelengths, a window of microwave frequency between 10 MHz to 2.5 GHz transmits through a body with negligible absorption and high penetration depth. This property of microwave energy is used in thermal treatment and diagnostic applications in biomedicine. Superparamagnetic iron oxide nanoparticles (SPION), gold nanoparticles (AuNPs) with about 10 nm diameter, and gold nanoclusters (AuNCs) with size about 2 nm potentially can be utilized for thermal conversion. The physical phenomena responsible for possible heat generation in SPIONs, AuNPs, and AuNCs are superparamagnetism, Surface Plasmon Resonance (SPR), and band splitting (between 5d and 6sp), respectively. Some studies have reported a temperature enhancement of SPIONs upon absorbing microwave energy [9-11]. In the case of AuNPs, no clear tests have been done in the field of microwave absorption. A review has presented the concept of radio frequency-to-thermal conversion of colloidal gold [12]. However, recently Kim et al. found the negligible absorption of the radio frequency (and microwave energy) by gold nanoparticles [13]. There is a knowledge gap in the case of AuNPs microwave absorption that raises the need for further investigation. Simple Mie modeling can predict the absorption of AuNPs in microwave range. Thus, absorption modeling of gold nanoparticles seems to be a reliable method capable of clarifying this issue. AuNCs have supramolecular properties and may offer some absorption in microwave region. However, this property has not theoretically or experimentally been studied yet.

In addition to investigating the thermal conversion properties of nanoparticles, the feasibility of using nanoparticles as contrast agent in a thermoacoustic tomography (TAT) system studied. TAT is a hybrid biomedical imaging modality based on the generation of thermoacoustic waves via microwave irradiation. In TAT imaging, radiofrequency or microwave pulses are delivered into biological tissues. Some of the delivered energy will be absorbed and converted into heat, leading to transient thermoelastic expansion and thus ultrasonic emission. The ultrasonic waves are then detected by ultrasonic transducers to form images. The applicability of SPIONs as

contrast agents in TAT due to high microwave absorption has been reported [9, 11]. However, more studies are needed to clarify the efficiency of SPIONs in absorption of microwave energy. In this research, the feasibility of using SPIONs, AuNPs, and/or AuNCs as hyperthermic and contrast TAT agents based on microwave absorption has been scrutinized.

1.2 Research Approach

Clarification of the microwave properties of AuNPs, AuNCs, and SPIONs for use as hyperthermic and contrast agents in TAT applications is the main goal of this research. To achieve this goal, AuNPs and SPIONs around 10 nm in diameter and AuNCs about 2 nm were synthesized. Nanoparticles were thoroughly cleaned from ionic solution left over in the synthesis process. Additionally, SPIONs were subjected to dialysis as well.

In the first step, different concentrations of SPIONs, AuNPs, and AuNCs were placed in microwave generator and exposed to microwave energy at 3 GHz with the same volume, power irradiation, and time duration. Then, the temperature enhancement of each sample was recorded. This process illustrated the ability of each sample to transduce microwave energy into thermal energy. The dielectric properties of materials (ratio of complex permittivity in material to that in vacuum) determine the absorption of microwave energy at various frequencies [14]. Thus, in the next step, the complex permittivity of each sample was measured by a dip probe kit and vector network analyzer (VNA) in a broad range between 500 MHz and 10 GHz. Through this measurement, the best frequency region with highest absorption spectrum was determined. Using the complex permittivity data, the absorption spectrum of each sample was calculated. Additionally, the absorption spectrum of AuNPs was simulated by using Mie's theory, as it is the only convenient solution to Maxwell's equation relevant to small particles. In the last step, each sample was tested as the exogenous contrast agents in a TAT system. Then, the thermoacoustic (TA) signal strength and TAT image contrast were compared with the results obtained from the first two parts. It

was expected that the nanoparticle sample that had the highest thermal efficiency and highest absorption spectrum would produce the strongest TA signal and thus highest contrast in TAT image.

1.3 Hyperthermia and TAT/PAT Description and Their Agents

Hyperthermia is a type of cancer treatment, in which abnormal cells will be damaged or killed by exposure to higher than normal temperatures. Cancer cells are more susceptible to hyperthermia effects than normal cells because of their higher metabolic rates [6, 15-17]. A marked reduction in tumor size after treatment by localized hyperthermia has been demonstrated by numerous clinical studies [5, 6, 18-20]. In hyperthermia as a treatment method, the target cells are heated between 41 °C to 47 °C, and for ablation of cancerous cells the target cells/tissue should be heated to the temperature above 47 °C (up to 57 °C) [21]. At temperatures between 37 °C and 41.5 °C (approximately), heat enhances cell growth and may cause the proliferation of tumor cells as well. Uniformly heating tumors without thermally enhancing the active growing edge of tumors, and at the same time not damaging the normal cells, needs the greatest degree in technological refinement. Furthermore, the thermoregulatory effect of the blood flow is another issue that must be considered. This effect causes the time varying changes of temperature patterns [22]. To optimize the hyperthermia effect, three issues should be considered for widespread clinical use: 1- generation of temperature enhancement only within the target (tumor) cells leaving normal tissue (cells) unaffected. 2- Controlling the temperature of the target cells. 3- The homogeneity of temperature in the target volume [21]. Hyperthermia system equipment which provides lower temperature (up to 42.5° C), is relatively safe, but duration of the treatment is one hour or more. On the other hand, the systems that produce higher temperature can last less than one hour, but present wider injury to a tissue. Such systems have the advantage of treatment duration less than one hour [22].

Fig.1 shows the schematic diagram of a typical electromagnetic hyperthermia induction system [22]. The electromagnetic induction system consists of a power generator, tuning and matching network, and applicator. The applicator directs energy to the target tissue. The bolus is used to improve the coupling between applicator and patient. The operation of the energy generator is controlled by the control subsystem which monitors temperature enhancement in different target locations and manipulates the power output to avoid overheating [22].
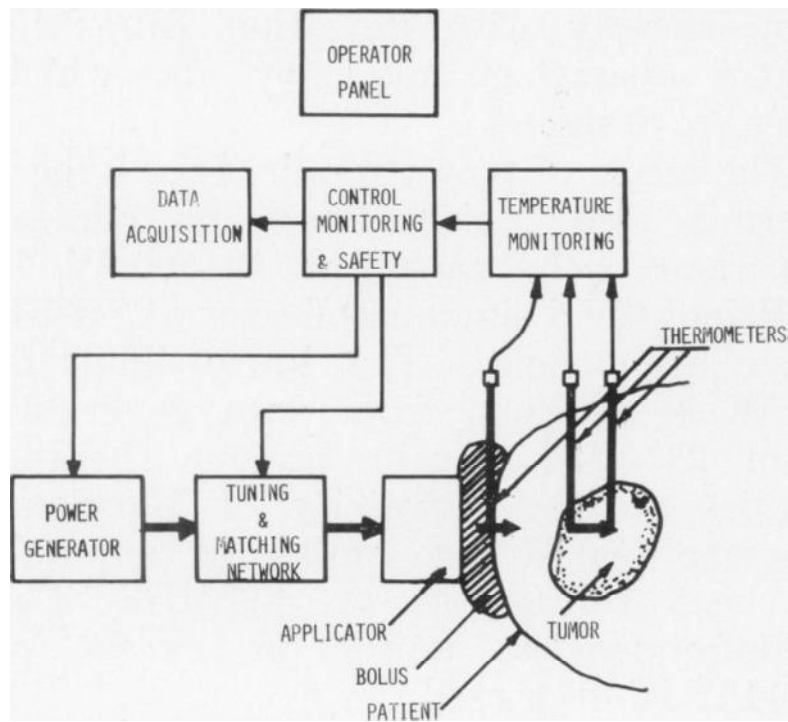

Fig. 1 Schematic diagram of a hyperthermia system [22].

There are two concepts behind the interaction of electromagnetic field which cause hyperthermia effects: 1- rotation of polar molecules and 2- oscillation of free electrons and ions. In the first case, the friction associated with the rotation of atoms and

molecules generates heats with the applied time varying electromagnetic field. In the second case, the collision between atom and ions within the molecule produces heat.

Materials which can generate heat by exposure to electromagnetic waves are characterized by dielectric property ε_r and conductivity σ of the material. The propagation of electromagnetic waves in the tissue is characterized by the reduced wavelength λ_{eff}, the absorption coefficient, absorbed power density P_a and power penetration depth D which related to ε_r and σ by:

$$\lambda_{\text{eff}} = \frac{\lambda_o}{\sqrt{\varepsilon_r}} \left(\frac{1}{2} - \frac{1}{2} \sqrt{\left(\frac{\sigma}{\omega \varepsilon_0 \varepsilon_r} \right)^2 + 1} \right)^{-\frac{1}{2}} \tag{1}$$

$$P_a = \frac{1}{2} \sigma |E|^2 \tag{2}$$

$$D = \frac{1}{2\alpha} \tag{3}$$

where ω is the angular frequency, λ_o is the wavelength in free space, E is the electric field, α is the absorption coefficient, and ε_r is the real part of dielectric constant. As ε_r and σ of the material are dependent to frequency, P_a and D are frequency dependent, accordingly. Fig. 2 represents the frequency dependence of the power density and penetration depth for two different tissues, muscle and fat [22]. The penetration is decreased at higher frequency which is reversed by diminished absorption coefficient. Therefore, increasing frequency range should be accompanied by an increase in power.
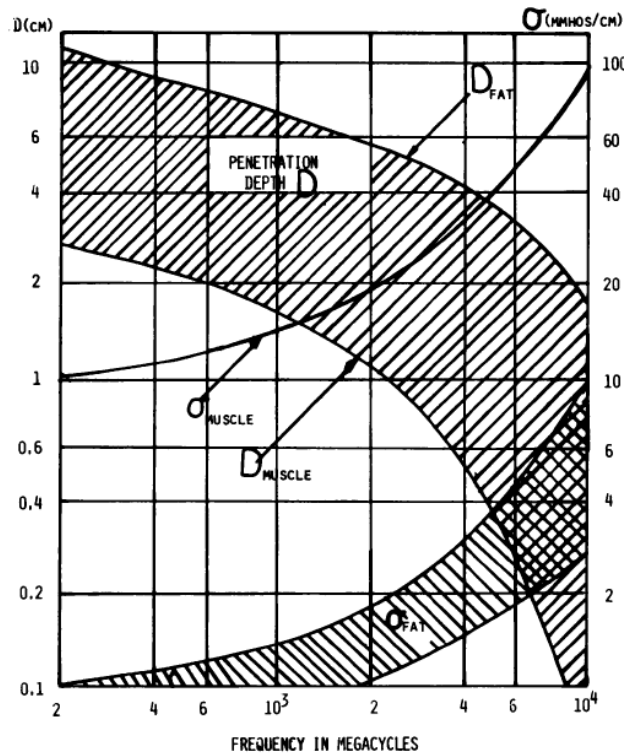
Fig. 2 Frequency dependence of penetration depth D and conductivity σ for fat and muscle tissues [22].

Photoacoustic tomography (PAT) is a hybrid method which combines high ultrasonic resolution and strong optical contrast in a single modality based on the photoacoustic effect. In PAT, Light absorption by molecules (or contrast agents) creates a thermally induced pressure change that launches ultrasonic waves which will be received by acoustic detectors to form images [15, 23, 24]. The optical absorption in biological tissues can be due to endogenous molecules, such as hemoglobin or melanin, or exogenous contrast agents, such as gold nanorods and gold nanocages [25, 26]. When radio frequency pulses or microwave energy are used as the source, the technology is referred as thermoacoustic tomography (TAT) [27]. Microwaves operate on the order of centimeters, rather than nanometers for light sources and have been used for medical imaging for several decades [18, 27-30]. TAT advantages over conventional imaging techniques such as X-ray, ultrasound and magnetic resonance are the

8

application of non-ionizing radiation, enhanced contrast for many important tissue structures, and relatively low cost (compared to magnetic resonance). TAT combines the advantages of pure optical imaging with those of ultrasound; whereas in optical imaging the contrast is usually high with low penetration depth due to the diffusion nature of light propagation. Although using longer wavelength in microwave imaging improves the penetration depth, it results in poor resolution. The transduction of electromagnetic waves into sound waves compensates for the loss in excitation resolution and makes TAT able to form images with high contrast and resolution [31]. Acoustic waves usually travel approximately 1.5 mm/μs in soft tissue and, at MHz frequencies, can provide excellent spatial resolution of 1mm or better [32]. TAT method has been used for many medical diagnostic applications. In humans, TAT has been used for mammography [33-35], examination of skin vasculature, monitoring the changes induced by heat in tissues, and imaging of tumors [36]. Also, TAT is capable of providing chemical information about the tissue as the amplitude of acoustic signal is dependent on the absorption coefficient [37]. For image reconstruction, the inverse problem of thermoelastic sound generation has to be solved. Detecting acoustic waves outside the sample allows the reconstruction of energy density distribution. In the literature, the analytical formula to calculate density functions has been derived from different detector assays such as planes, sphere, cylinder and circle [38-40]. To achieve high spatial resolution throughout the three dimensional image space, the ultrasound detectors that are much smaller than the object must be used [36].

The electric field as a plane wave in a medium is propagated and attenuated as:

$$E = E_0 e^{j\omega t - \gamma(\omega)z} \tag{4}$$

where E is the electric field of a distance Z from the electric source E_0. The propagation constant $\gamma(\omega)$ is equal to $\gamma(\omega) = \alpha(\omega) + \beta(\omega)$ where $\alpha(\omega)$ and $\beta(\omega)$ are the attenuation constant and phase constant at angular frequency, respectively. The total rate of absorbed energy by the sample will be defined by specific absorption rate (SAR) which can be written as:

$$SAR = \sigma \, |E|^2 \, / \, \rho \qquad\qquad\qquad (5)$$

where ρ is the mass density and σ is the conductivity of the sample. Later on, in section 3.3, it will be shown that the attenuation constant can be defined by the dielectric properties of the sample. Thus, if we know the dielectric properties of a sample, we will be able to calculate strength of the electric field and conductivity to estimate the deposition of energy at specific location. In small samples, we can assume that the electric field is uniformly distributed in the sample to simplify the computation [9]. Since the attenuation of the electromagnetic field in a medium is due to electric loss, the $\alpha(\omega)$ will be used as the absorption coefficient of the medium.
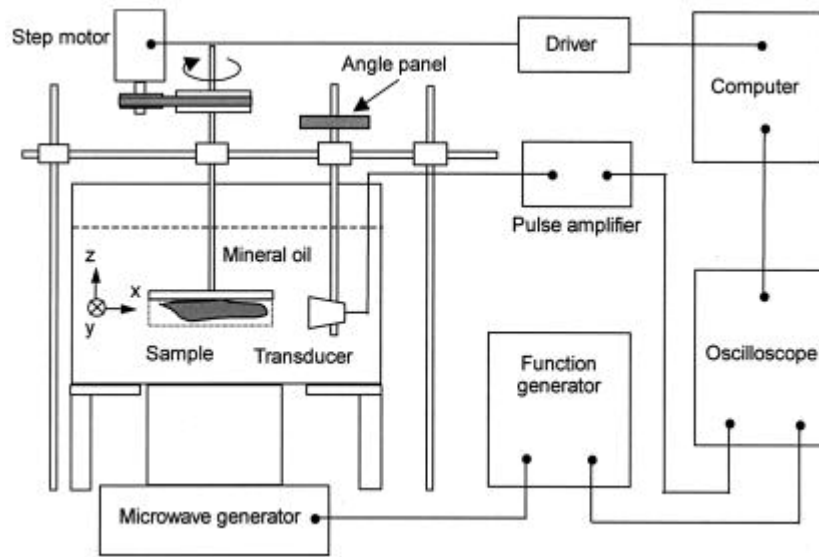

Fig. 3 TAT experimental set up for 2D imaging

TAT integrates rich microwave contrast and good ultrasound resolution in one imaging modality. Water and ions in tissue are the primary endogenous contrast agents. Water also limits the penetration depth. Exogenous contrast agents provide decoupled

10

contrast and high penetration depth from thermoacoustic signals. Recently, iron oxide nanoparticles have been used as contrast agents in thermoacoustic tomography. [9, 11, 27, 29].

In the implementation of TAT, the sample is placed in a mineral oil bath. The reason is that mineral oil has relatively low microwave absorption and high penetration depth, which allows the microwave energy to reach the sample. Also, acoustic waves can easily travel through the medium to be detected by the transducer.

There are two modes in the implementation of a TAT system. The first mode is the forward mode, in which the irradiation source and detector are placed on the opposite sides of the sample. Conversely, in the backward mode, both the irradiation source and the detector are on the same side of the sample. Most TAT instruments consist of some common components. A computer is used to store the data collection and control the movement of ultrasonic detector. This computer also is connected to a function generator to trigger microwave source and synchronize the oscilloscope during the experiment. The detected signal by the transducer is usually in the µV range, and therefore, must be amplified by a pulse amplifier. The signal detected by transducer is send to the pulse amplifier and recorded by computer. Then, the signal averaged 200 times by oscilloscope and data will be store in the computer.

After the experiment completed, the 1D data from transducer can be combined to create a 2D image (Fig.3). It should be noticed that that the boundaries that are parallel to the transducer will not be observed. In other words, the transducer only detects boundaries which are perpendicular to transducer. To improve the image quality, the transducer can rotate around the sample.

1.4 Superparamagnetic Iron oxide Nanoparticles (SPIONs)

Magnetic materials can be found in a variety of applications that range from microelectronic devices to motors and power distribution systems. Recent advances in

colloidal synthesis have greatly enhanced the ability to manipulate the magnetic properties of materials, particularly at the nanometer scale, and enabled many innovative biomedical applications including cell labeling, imaging, and site-specific drug delivery [41, 42]. The attractive or repulsive forces between magnetic materials can be described in terms of magnetic dipoles—tiny bar magnets with opposite poles. Materials can thus be classified as diamagnetic, paramagnetic, ferromagnetic, and ferrimagnetic according to the arrangement of their magnetic dipoles in the absence and presence of an external magnetic field. If a material does not have magnetic dipoles in the absence of an external field and has weak induced dipoles in the presence of a field, the material is referred to as diamagnetic. If a material has randomly oriented dipoles that can be aligned in an external field, it is paramagnetic. The magnetic interactions derived from the above two types of materials are very weak. For a ferromagnetic material, the magnetic dipoles always exist in the absence and presence of an external field and exhibit long-range order. Macroscopically, such a material displays a permanent magnetic moment. Both ferro- or ferrimagnetic materials can be described using a number of basic parameters derived from the magnetization curve where the magnetization M or flux density B is plotted against the magnetic field strength H. Magnetism is highly size and temperature dependent because this property arises from the collective interaction of atomic magnetic dipoles.

When the size of a ferro- or ferrimagnet decreases to a certain critical value r_c, the particles change from a state with multiple magnetic domains to one with a single domain. Such small particles do not have permanent magnetic moments in the absence of an external field but can respond to an external magnetic field. They are referred to as superparamagnetic particles. An important parameter to describe superparamagnetic colloids is the blocking temperature (T_B); the transition point at which the thermal energy kT is comparable to the magnetic anisotropy energy or the energy barrier for spin reorientation. The blocking temperature is determined experimentally from the magnetization-temperature curve using a magnetometer. Superparamagnetic colloids have found widespread use in many traditional areas including magnetic data storage,

ferrofluid technology, magnetorheological polishing, and energy storage; they also hold great potential for many other applications related to biomedical research [41]. To this end, superparamagnetic colloids have been exploited for labeling and separation of DNA, proteins, bacteria, and various biological species, as well as applied to magnetic resonance imaging (MRI), guided drug delivery, and hyperthermia treatment of cancer [41]. Certain types of molecular interactions can also be probed *in vivo* using specially designed magnetic probes. For *in vivo* applications, the magnetic particles must be coated with a biocompatible polymer during or after the synthesis process to prevent the occurrence of large aggregates, structural changes, or biodegradation when exposed to the biological system [43, 44].

The important factors which determine the biocompatibility and toxicity of these materials include the nature of the magnetically responsive component, such as iron, nickel, cobalt, the final size of the particles, and their coatings. Iron oxide nanoparticles in magnetite forms (Fe_3O_4) are by far the most commonly employed superparamagnetic nanoparticles approved for *in vivo* applications. Highly magnetic materials such as cobalt and nickel are toxic and susceptible to oxidation and, hence, of little interest [26]. Other advantages of using particles with sizes smaller than 100 nm are their higher effective surface areas (easier attachment of ligands) and lower sedimentation rates (high stability) [45]. Finally, the magnetic dipole–dipole interactions are significantly reduced because they scale as r^6 (r is the particle radius) [45, 46]. The applicability of magnetic nanoparticles can be categorized into *in vivo* and *in vitro* applications. For *in vivo* biomedical applications, magnetic nanoparticles must be made of a non-toxic and non-immunogenic material with particle sizes small enough to remain in the circulation after injection and to pass through the capillary systems of organs and tissues avoiding vessel embolism [46]. For *in vitro* applications the size restrictions are not as severe as *in vivo* applications. Therefore, composites consisting of superparamagnetic nanocrystals dispersed in submicron diamagnetic particles with long sedimentation times in the absence of a magnetic field can be used. *In vivo* applications include therapeutic such as hyperthermia and diagnostic fields, while the main application of *in vitro* is diagnosis.

Some studies have revealed that SPIONs have the potential to convert microwave energy into the heat [9-11]. By choosing a reasonably high power source at commercially available microwave energy, 2.45 GHz, the temperature rise behavior of SPIONs can be studied. The temperature enhancement of SPIONs exposed to microwave energy at 2.45 GHz versus time and concentration is shown in Fig. 4.

It has been demonstrated that at frequencies between 200 MHz to near 3 GHz water has low absorption while SPIONs absorb effectively [9]. Working in this window, we can take advantage of higher penetration depth due to small water absorption. The microwave absorption spectrums of water and 10 nm SPIONs is presented in Fig. 5.

As already discussed by other researchers, SPIONs have been used as exogenous contrast agents in TAT systems [9]. Fig.6 (a) shows a reconstructed TAT image using SPIONs as contrast agents. In this figure, white arrows denote two tubes filled with SPIONs while black arrows mark two tubes filled out with deionized water. As the figure demonstrates, SPIONs provide higher contrast compared to water [9]. Fig.6. (b) illustrates the brightly visible thermoacoustic image of the mouse tail after injection of Fe_3O_4/PANI contrast agents with three times greater contrast enhancement than the control image without any contrast agents [11].

Although some reports have addressed the microwave absorption by SPIONs and significant temperature enhancement, systematic investigation is required to measure the amount of microwave-induced heat contributed by SPIONs. This is critical to explore the applicability of the SPIONs in conversion of microwave energy to thermal effect, thermoelastic expansion, and ultrasonic wave generation.
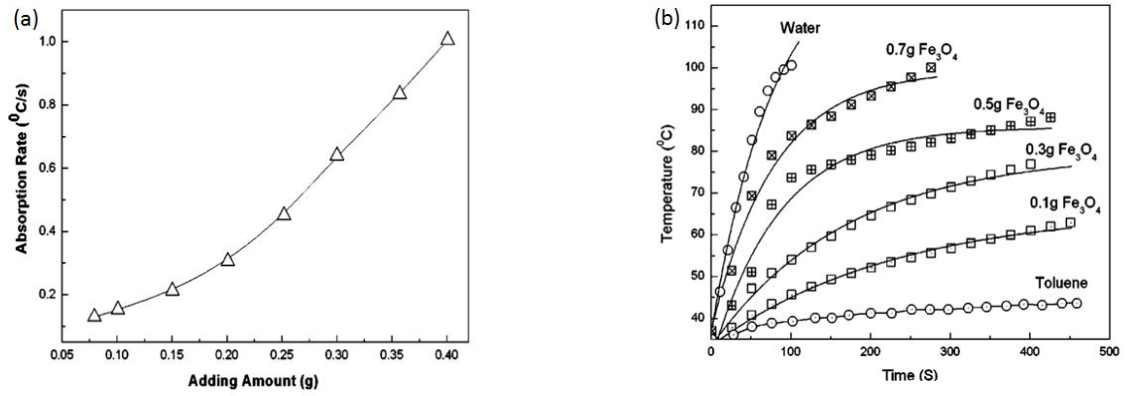
Fig. 4 Microwave properties of SPIONs. (a) microwave absorption of 11nm SPIONs at 2.45 GHz. (b) Temperature profile of different concentration of Fe_3O_4 exposing to 2.45 GHz microwave energy [10].
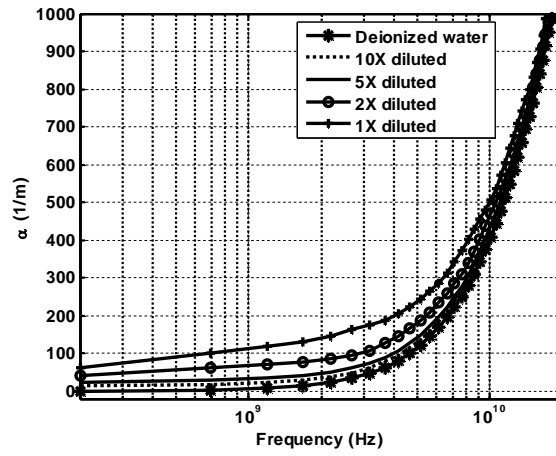

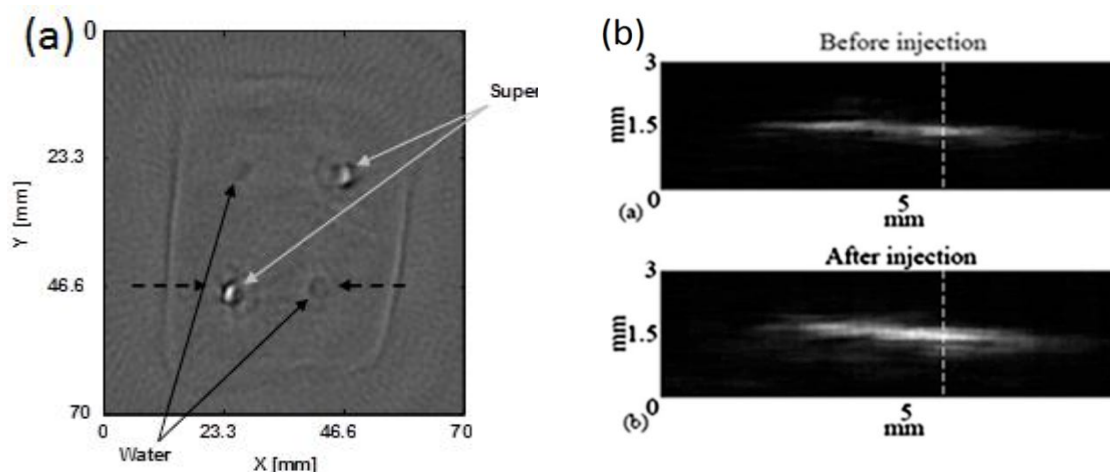Fig. 5 Absorption spectrum of 10nm SPIONS versus frequency [9].

Figure. 6 TAT images of SPIONs. (a) Reconstructed TAT image. Bright spots marked with white arrows shows the higher contrast efficiency provided by iron oxide nanoparticles (supernatant) in comparison with water, marked with dark arrows [9]. (b) *In vivo* TAT imaging of a mouse tail before and after intravenous injection of Fe_3O_4/PANI as the contrast agents [11].

1.5 Gold Nanoparticles (AuNPs)

AuNPs, which have been known for over 2500 years, are promising medicate therapeotics because they are biocompatible, simple prepared and bioconjugated. In 1857, Faraday reported the formation of red colloidal gold by reduction of chloroaurate ($AuCl_4^-$) using phosphate in CS_2 in a well-known experiment. He also reported the optical properties and reversible color of thin gold film by drying the colloidal gold solution via mechanical compression (from dark bluish purple to green). The term "colloid" was used shortly thereafter by Graham in 1861 [47]. In 1908 Mie described the phenomena by solving the Maxwell equation to describe the extinction spectra (extinction=absorption+ scattering) of spherical particles. In this approach, the dielectric constants of both the particles and the medium in which the particles are embedded must be known [48]. Mie's solution remains of great interest to this day, as it is the most convenient solution to Maxwell's equations which is relevant to particles. Also, most of colloidal preparation yields particles that are approximately spherical, and most of

optical characterization methods probe a large ensemble of particles. This indicates that experimental results can be well modeled using Mie's theory [49].

In AuNPs, which vary in size from 3nm up to 100 nm, optical processes interfacing with particles (such as absorption) are enhanced strongly due to the unique interaction of light with the free electrons in AuNPs. The conduction band electrons of AuNPs are free to travel through the material with a mean free path in gold of about 50 nm. When the wavelength of incident light is much larger than particle size, the electron density in the particle is polarized and starts to move with the light's frequency. At a suitable wavelength, resonant dipolar and/or multipolar modes can be excited in the nanoparticles, which lead to a significant enhancement in absorbed and scattered light. This phenomenon is referred to surface plasmon resonance (SPR). The distinctive colors of AuNPs, are attributed to the presence of this surface plasmon absorption [7, 50]. The resonance condition of free electrons is sensitive to changes in the size and shape of the particle. As the diameter gets smaller the energy required to excite the surface plasmon electrons increases [51]. For AuNPs with size near 10 nm in diameter, the energy required to excite the surface plasmon is comparable to the energy of visible light. Thus, the particles strongly absorb at visible wavelengths with a maximum absorbance near 520 nm, giving rise to the brilliant red color of the colloidal gold solution. AuNPs with different sizes have specific absorption spectra related to surface plasmon resonance. When the diameters of nanoparticles is between 12 and 41 nm, the maximum absorption peaks is in the 520-530 nm range and gradually red shifts with increased of diameters of gold nanoparticles (Fig.7) [52].
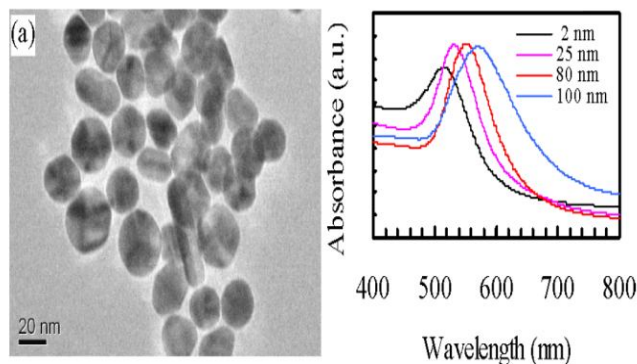
Fig. 7 TEM image and optical absorption of AuNPs with different sizes [5].

When AuNPs are irradiated at resonance, they absorb energy, which is quickly transferred through non-radiative relaxation into heat and accompanied effects. This may lead to irreparable damage into cell membranes given sufficient temperature rise. The reason that AuNPs are promising candidates for such hyperthermia treatment is their high absorption coefficient due to SPR [5]. The maximum absorption of AuNPs can be shifted to the near-infrared spectral range (700–900 nm). This allows penetration of the laser radiation into biotissues up to few mm deep due to scattering and attenuation of near-infrared light by biological tissues [53, 54]. Recently, it was shown that AuNPs heat under radiofrequency fields [12, 53, 55]. Radiofrequency (3MHz-300MHz) heating of AuNPs within cancer cells can overcome the major limitations associated with other noninvasive nanoparticle heating methods, since radiofrequency energy penetrates well into the body to efficiently heat AuNPs within deep tissue tumors. Fig. 8 (a) plots the change in temperature versus time for selected concentrations of 10 nm AuNPs in diameter exposed to radiofrequency fields at 13.56 MHz. DI-water alone and physiological saline (not shown in the figure) exhibited a 5 °C rise from room temperature over a 2-min period. For the maximum concentration (36 ppm) of 10 nm gold nanoparticles, the heating rate is 3.4 °C/s, which corresponds to a 70-fold increase in the thermal power dissipation by AuNPs as compared to water alone [12]. However,

the role of gold AuNPs in radiofrequency heating was poorly understood until Kim *et al.* systematically investigated negligible absorption of AuNPs in radiofrequency irradiation. Here, AuNPs were cleaned carefully by centrifugation. Radiofrequency testing of the AuNPs-separated (and resuspended in DI-water) solution clearly revealed that they do not contribute to heating. Instead the dipolar heating of residual ions from AuNPs synthesis (ionic conductivity) caused the radiofrequency heating reported before (Fig. 8 (b)) [13]. When AuNPs are exposed to microwave or radio frequencies, the molecular dipoles of the material align in the applied electric field. As the applied field oscillates, the dipole field attempts to follow these oscillations and the energy is lost in the form of heat. The amount of heat generated by this process is directly related to the ability of the molecules to align themselves with the frequency of the applied field. In this step, simple Mie modeling can predict whether the claims on radiofrequency and microwave heating of AuNPs solutions are reliable.
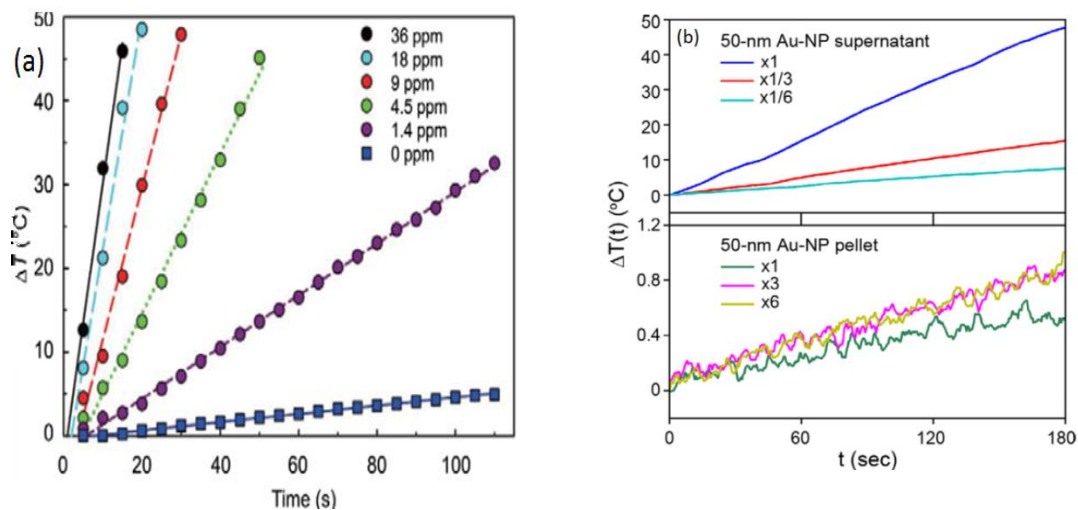

Fig. 8 RF heating of AuNPs by exposing to 13.56 MHz radiofrequency energy. (a) Significant temperature enhancement of nanoparticles by increasing concentration [12]. (b) Negligible temperature enhancement of AuNPs by increasing concentration exposing to 13.56 MHz field [13].

1.6 Gold Nanoclusters (AuNCs)

Noble metal nanoclusters, such as AuNCs with size below 2.5 nm, have attracted interest for their unique and important role in bridging the gap between atomic and nanostructure behavior (Fig. 9) [56]. In spite of the advantages of QDs in luminescent labeling, cancer targeting and imaging, toxicity of QDs makes them unsuitable for *in vivo* clinical applications [57]. In contrast to QDs, noble metal nanoclusters, such as AuNCs, are highly attractive for bioimaging applications due to their low toxicity as well as their ultrafine size. Recent research has been focused on the AuNCs quantum opto-electronic properties such as photoluminescence [58]. This is based on the size-dependent properties of the clusters.

Fig. 9 Metal nanoclusters fill the gap between molecular chemistry and nanocrystals. The scale bar is 5 nm [59].

To understand the fundamental properties of metal nanoparticles, the free electron theory provides insight into electronic properties of metal nanoparticles. It should be noted that the free electron model only serves for estimation purposes and it does not

take into account the surface effect in small particles and ligand's contribution to the electronic structure. Bulk metals typically have cubic or hexagonal structure such as fcc, bcc, and hcp. Because of high electron density in bulk metals such as gold, the electron states are densely spaced and form quasi continuous band (e.g 6s to 6sp bands and 5d bands). By the first order approximation of the free electron theory, the 6s band can be well described. In the band theory, the rigorously computed s band (6s for gold) closely resembles what is derived from the free electron model. In AuNPs, the electronic conduction band consists of quasicontinuous energy levels (i.e. spacing $\delta \ll K_BT$, where K_BT is the thermal energy at temperature T (typically room temperature) and K_B is the Boltzmann constant). Electrons in the conduction band roam throughout the gold, and light can collectively excite these electrons to give rise to plasmonic responses (SPR). On the other hand, when gold nanoparticles become extremely small (<2 nm in diameter), significant quantization occurs to the conduction band. Gold nanoclusters have discrete electronic energy levels as opposed to the continuous band in plasmonic nanoparticles (AuNPs). Quantum-sized nanoparticles also show multiple optical absorption peaks in the optical spectrum versus a single surface plasmon resonance (SPR) peak at 520 nm for spherical gold nanocrystals. Although AuNPs show an fcc structure, AuNCs often have non-fcc atomic packing structures. Due to the strong quantum confinement effect, adding or removing one gold atom significantly changes the structure and the electronic and optical properties of the nanocluster. Therefore, precise control of the number of atoms in the particle becomes necessary [60]. In AuNCs, the number of atoms in the particle is finite, thus the spacing δ becomes appreciable, increasing with decreasing the size of particle. By using thermal energy (K_BT) at room temperature (~ 273 K) and using equation below, we can estimate at what size the electronic energy quantization is comparable to thermal energy:

$$\delta = K_BT \tag{4}$$

By substituting all constant and highest occupied energy level of gold (Fermi level which is equal to 5.5 eV or 8.8×10^{-27} J) the corresponding size of the particle volume is

~ 5×10^{-27} m^3 which is equivalent to ~1.7 nm or roughly 2 nm. This gives the critical particle size at which electronic energy quantization becomes important. Indeed, at this size and smaller, the particle no longer possess plasmon resonance and Mie theory can no longer predict properties. In fact, small AuNCs have sizes comparable to the Fermi wavelength (ca. 0.7 nm), resulting in molecule-like properties such as discrete electronic states and photoluminescence [58, 59, 61, 62].

Fig. 8 shows the molecular orbitals (MO), energies, and atomic orbitals (AO) contribution of AuNCs (Au$_{25}$(SH)$_{18}$) by Kohn-Sham [5]. In the electronic structure of (Au$_{25}$(SH)$_{18}$), the highest occupies molecular orbital (HOMO) and the three lowest unoccupied molecular orbitals (LUMO) are mainly composed of 6s (6sp) atomic orbitals which is labeled in green. The HOMO bands are nearly triply degenerate while LUMO band is double degenerate. The HOMO-1 through HOMO-5 are constructed from 5d^{10} bands in the gold, thus constitute d bands of gold. Both sets of HOMO and LUMO orbitals have significant degree of S(3p) character (labeled in orange in Fig.8). This indicates that ligands influence the electronic structure of the cluster. The HOMO-LUMO gap (1.3 eV) agrees well with the experimental results [63, 64]

The optical properties of AuNCs are one of the most interesting material properties. A precise correlation of the Au$_{25}$ in the Au$_{25}$(SR)$_{18}$ structure with its optical absorption properties was obtained [64]. The theoretical spectrum of Au$_{25}$(SR)$_{18}$ is similar to the experimental absorption spectrum (Fig. 10 (b) and Fig. 11, respectively). The first excited transition occurs at 1.52 eV (peak a in Fig. 10 (b) and Fig. 11 which is corresponds to HOMO-LUMO transition in Fig.10 (a). There are only three HOMO orbitals that have more s character than d character; thus, all the transitions arising out of the other occupied HOMO$_{-n}$ orbitals tend to interband transition, which corresponds to pack b at 2.63 eV in Fig. 10 (b) and Fig. 11 (d to sp transition). Also, the peak labeled c in Fig.10 (b) and Fig. 11 arises from an interband transition (d to sp) which is equal to 2.91 eV.

Link *et al.* reported that photoluminescence of Au $(SG)_{18}$ (corrected formula) can be divided into two bands with peck at around 1.15 eV and 1.5 eV [65]. Bigioni and Whetten also reported near infrared emission (1100-1600nm) from various clusters with different sizes (1.1-1.7 nm) using a 1064 nm excitation source [66]. The mechanism for the luminescence is hypothesized to be associated with interband transition between the filled 5d band and 6sp conduction band [67-69].

As mentioned in section 1.1, heat generation by exposing nanoclusters to microwave energy might take advantage of subconduction band transitions between 5d and 6sp (Fig. 10). In this case, microwave energy can be absorbed between these bands which may cause conversion of absorption to thermal energy. Exposing AuNCs solution to microwave energy and obtaining significantly increased in temperature may prove the existence of real subconduction bands.
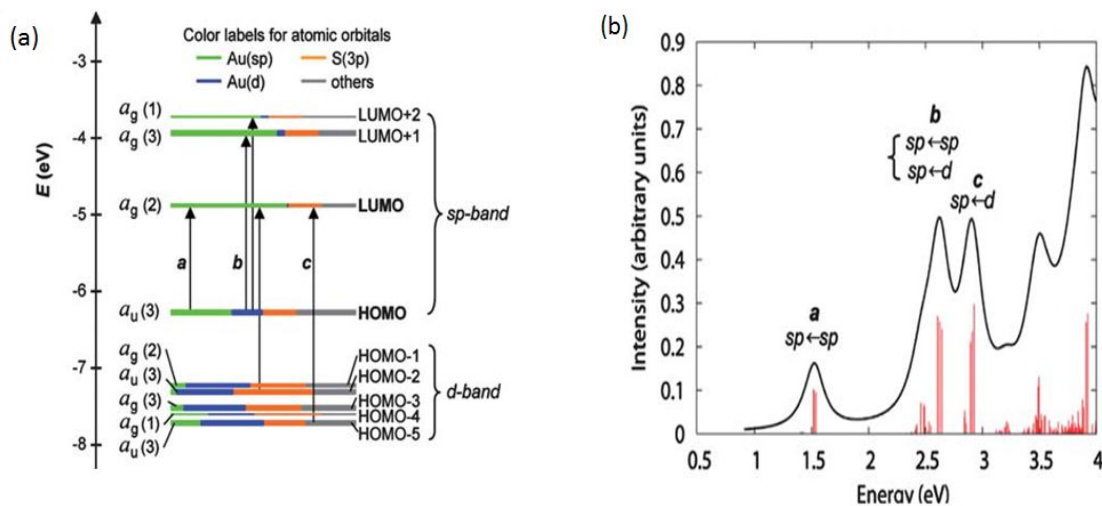

Fig. 10 Energy diagram of AuNCs. (a) Kohn-Shan orbital energy diagram for a compound gold nanoclusters ($Au_{25}(SH)_{18}$). Each Ks orbital is drawn to indicate relative contributions (line length with colored labels) of atomic orbital of Au (6sp) in green, Au (5d) in blue, S(3p) in yellow, and others in grey. (b) Theoretical absorption spectrum of $Au_{25}(SH)_{18}$ [59].
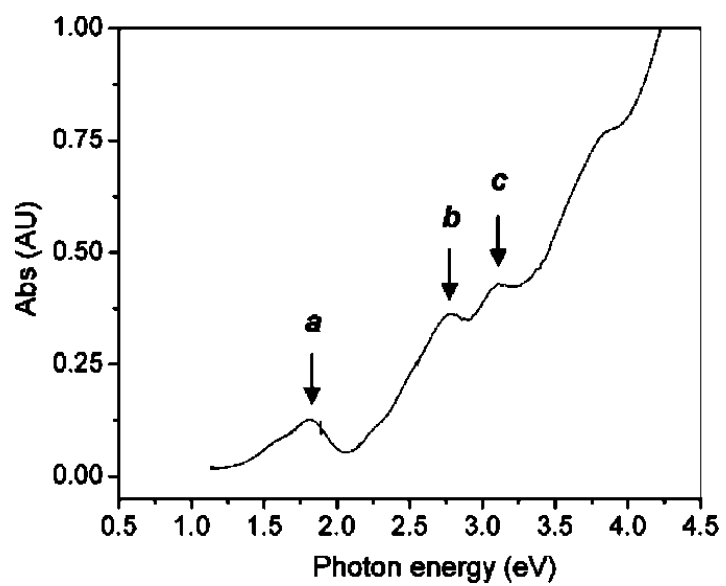
Fig. 11 UV-vis spectrum of Au$_{25}$ clusters [64].

CHAPTER II

SYNTHESIZATION AND CHARACTERIZATION OF NANOPARTICLES

2.1 Synthesize of SPIONs

The co-precipitation method is chosen to make SPIONs as it is the most effective technique for preparing aqueous dispersion of iron oxide nanoparticles [70]. In a typical reaction, 0.86 gr $FeCl_2$ and 2.35 gr $FeCl_3$ were mixed in 40 ml water and heated to 80º C under argon gas in a three-necked flask. While vigorously stirring the reaction mixture, 5 ml of NH4OH was introduced by syringe and heated for thirty minutes. Subsequently, 1g of citric acid (CA) in 2ml water was added, then the temperature increased to 95º C and the solution was stirred for ninety minutes. The experimental set up is shown in Fig. 12 (a). A small aliquot of the reaction mixture was withdrawn, diluted to twice its volume and placed on a 0.5 Tesla magnet in a vial. If the particles did not settle down under the influence of the magnet, the colloidal solution was stable and the experiment was complete. The as-formed reaction product contained an excess of citric acid. Therefore, the nanoparticle dispersion were subjected to dialysis against water in a 12-14 kD cut-off cellulose membrane for 72 hours to remove the excess unbound CA [71]. Then, the nanoparticles were purified by triple ultracentrifugation and washed by DI-water (Fig. 12 (b)).
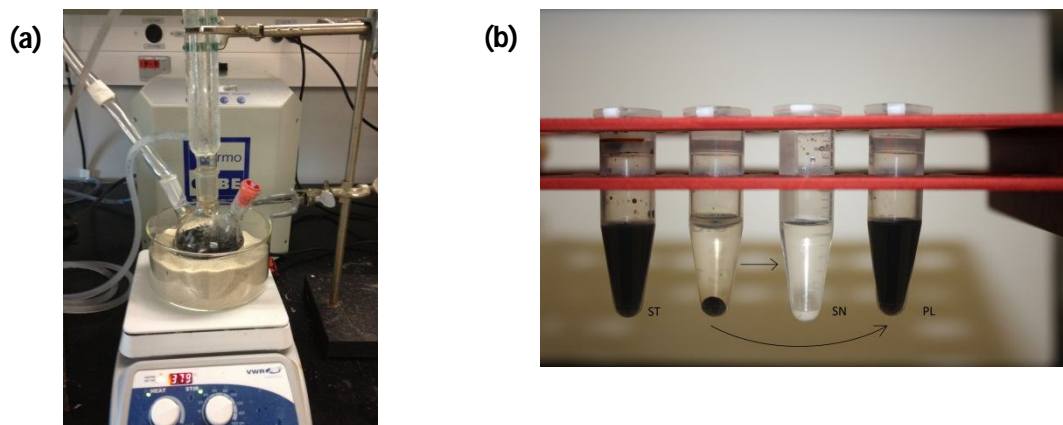
Fig. 12 Synthesis and preparation of SPIONs. (a) Experimental set up of SPIONs synthesis. The reaction kep under argon gas during the process to prevent oxidation. (b) Centrifugation of SPIONs solution after dialysis and re-suspending pellet part to DI-water.

2.2 Synthesize of AuNPs

All the glassware in this synthesis should be cleaned with aqua regia solution (HCL: HNO_3, 3:1 by volume). To prepare 10 nm gold nanospheres, a 50 ml, 1 mM solution of gold made with 19.7 mg of gold tetrachloroaurate trihydrate. The solution was heated to a boil. Then 9 ml of 38.8 mM citrate solution swiftly injected. The mixture was clear initially and eventually turned into deep red, signaling the formation of AuNPs [72]. To eliminate the ionic constituent left over in the synthesis process, AuNPs cleaned by triple ultra-centrifugation and were resuspended into DI- water. The synthesis process is shown in Fig. 13.
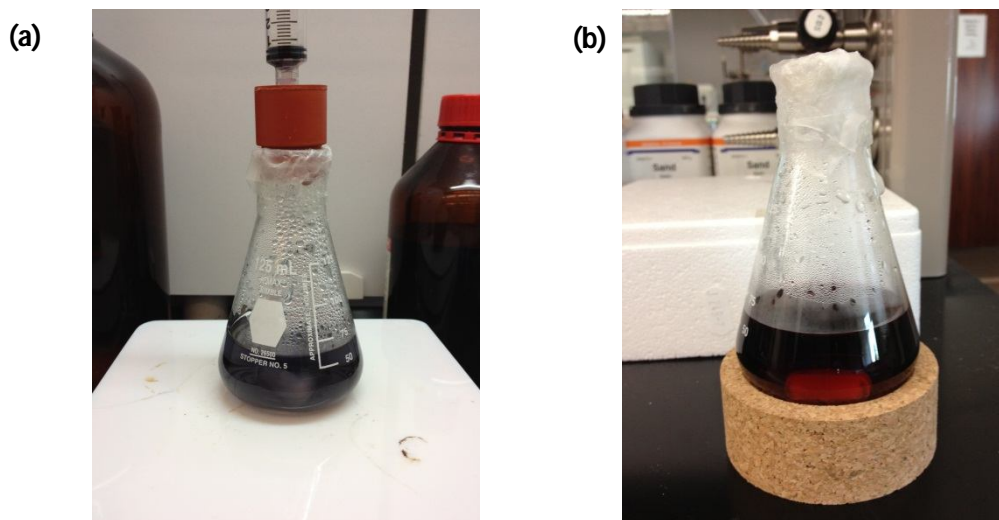
Fig. 13 The synthesis process of AuNPs. (a) Injection of citrate changes the color of solution from yellow to clear, and then blue. (b) after few minutes of injecting citrate, the solution turns deep red, signaling the formation of AuNPs.

2.3 Synthesize of AuNCs

All glassware in this synthesis should be cleaned in a bath of freshly prepared aqua regia and rinsed thoroughly in Millipore water prior to use. Lipoic acid (1.3 mg) was added to 3.9 ml aqueous solution containing 10 µl NaOH (2M). The mixture was stirred for 15 minutes and followed by addition of a solution of $HAuCl_4$ (40µl,2% by mass). Then, the solution turned from light yellow to colorless to upon stirring for another 5 minutes. Subsequently an aqueous solution of sodium borohydride (80 µl, 50 mM) introduced slowly to the mixture under rapid stirring. The reaction, which turned the colorless solution pale brown, was stopped after stirring overnight. The synthesis process is shown in Fig. 14. AuNCs were purified by triple centrifugation filtration; using Nanosep filters (Pall Nanosep, Ann Arbor, MI) with a molecular weight cut-off 10 kDa to remove impurities and resuspended to DI-water (Fig. 15). For later use, the solution were stored at $4°C$ [73].
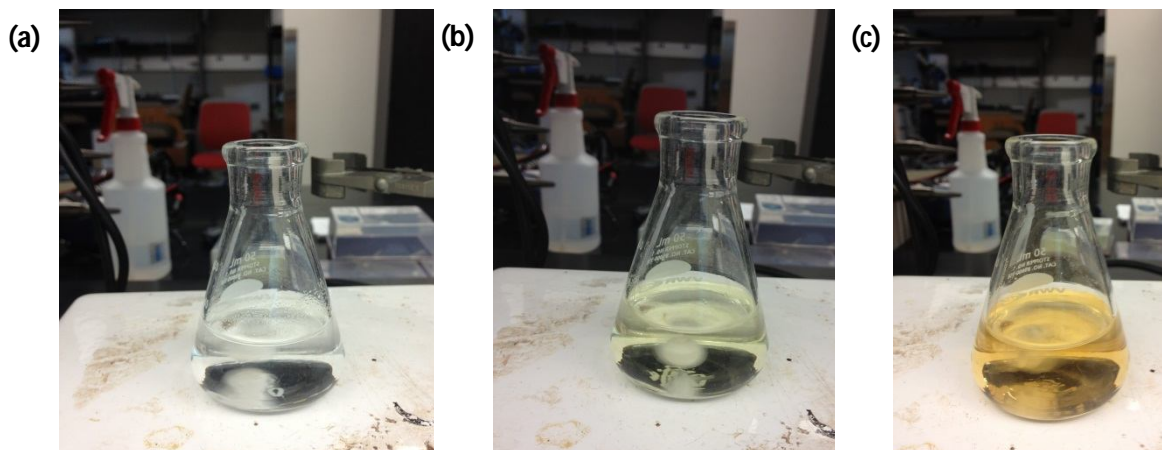
Fig. 14 The synthesis process of AuNCs. (a) Stirring lipoic acid for 15 minutes. (b) Addition of HAuCl$_4$ solution. (c) AuNCs solution after strring over night.
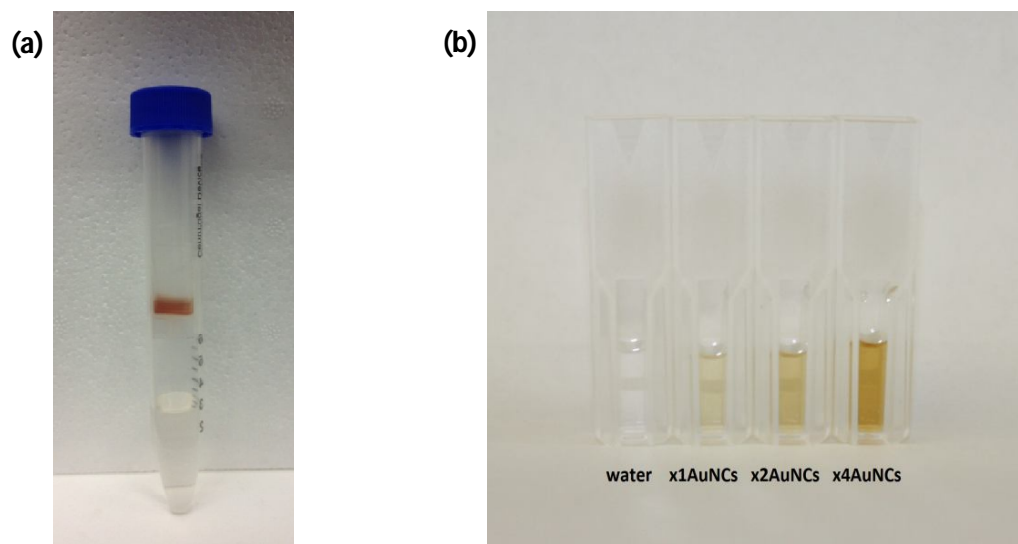

Fig. 15 Purification of AuNCs by ultra-centrifugation. (a) The AuNCs solution after synthesis was purified by using filter with a molecular weight cut off 10 kDa. (b) Then concentrated. The × 1 AuNCs, × 2 AuNCs, × 4 AuNCs, correspond to initial concentration, two times concentrated, and four times concentrated AuNCs solution respectively.

2.4 Characterization of SPIONs

After synthesis, small aliquots of the sample are taken for imaging. TEM images are taken to verify morphology of the SPIONs. For imaging, carbon film coated grids were glow discharged in an electric field. A drop of the colloidal solution was then deposited on the grid and allowed to evaporate. The TEM images of the SPION samples show particles size averaging about 10nm in diameter as represented in Fig. 16 (a) and Fig. 16 (b). Also, magnetic property of SPIONs is shown in Fig. 16 (c). In order to measure the concentration of SPIONs, three samples of 4×SPIONs with the volume of 0.5 ml (four times concentrated SPIONs after 96 hours dialysis time) were place in the vacuum heater to let the sample dry. After 25 minutes, the powder remained in the backer was measured for each sample. The weight average of three samples was 44 mg/ml. thus the initial concentration of SPIONs was 11 mg/ml.
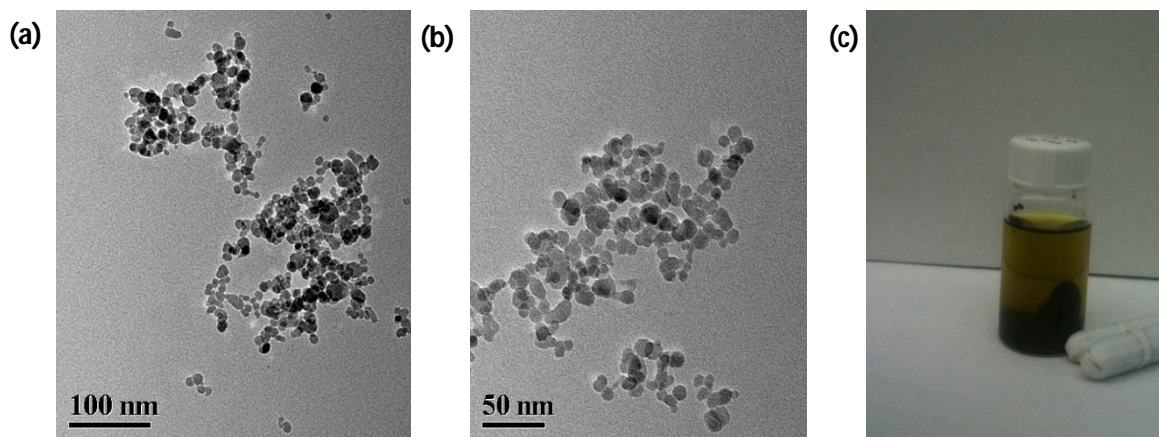

Fig. 16 Characterization of SPIONs. (a) TEM images of 10 nm SPIONs with size scale of 100 nm. (b) TEM images of 10 nm SPIONs with size scale of 50 nm. (c) SPIONs are attracted by magnetic stir bars.

2.5 Characterization of AuNPs

Optical absorption measurement of AuNPs was performed by Hitachi U-1400 UV-vis spectrometer. The absorption spectrum indicates that the surface plasmon resonance peak of AuNPs is positioned around 520 nm as shown in Fig. 17. Also, TEM images of AuNPs reveal spherical formation of AuNPs averaging at 12 ± 0.5 nm in diameter (Fig. 18). The concentration of AuNPs synthesized in the process explained in section 2.2 is equal to 0.2 mg/ml. It should be noted that by increasing the amount of gold salt in the synthesis process the size of AuNPs will change.
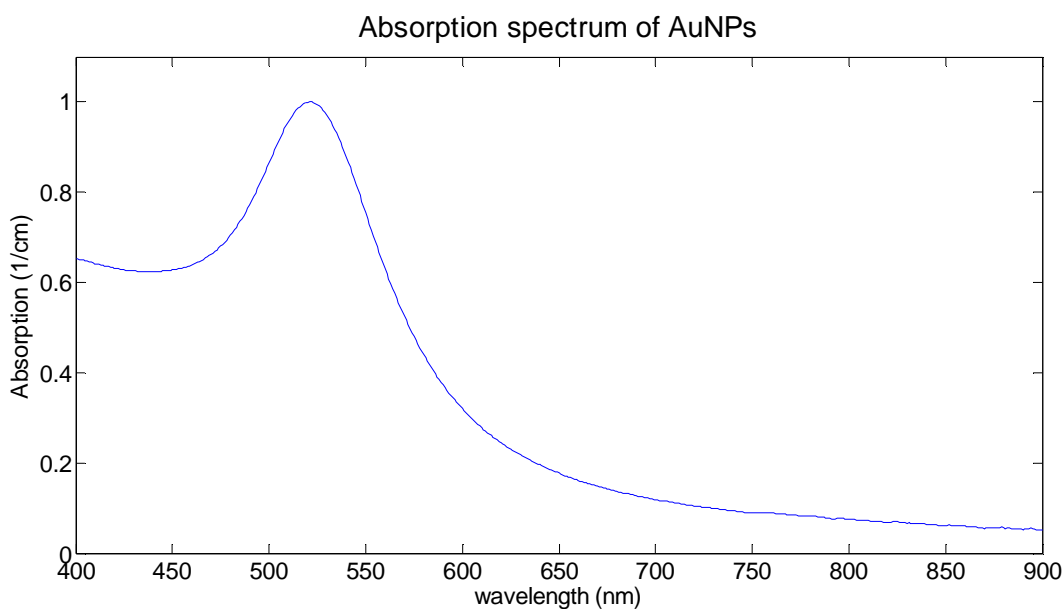

Fig. 17 UV-vis spectroscopy characterization of AuNPs. The figure shows the existence of surface plasmon resonance peak at 520 nm.
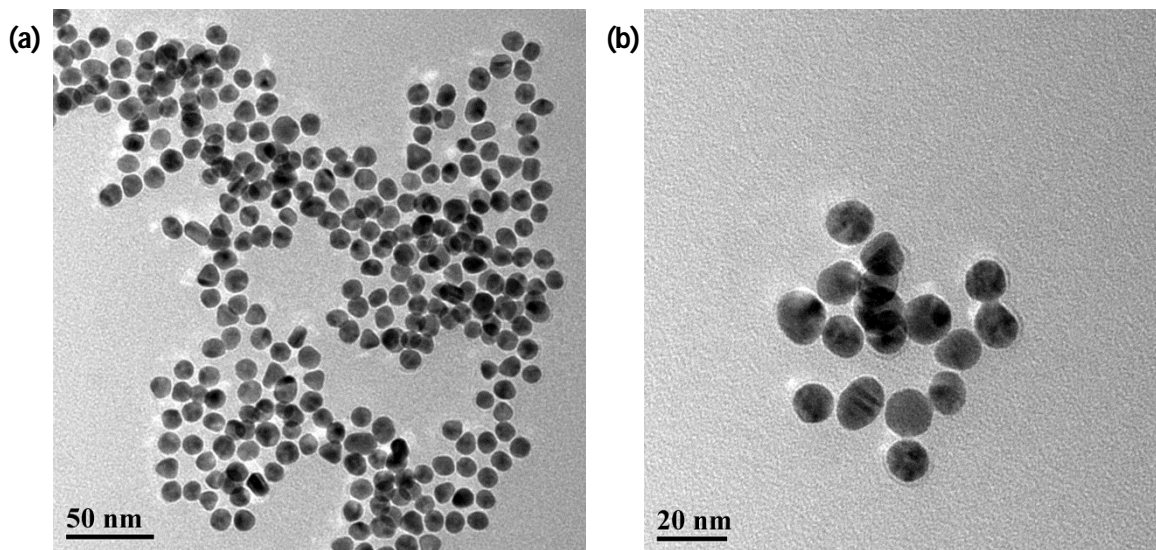
Fig. 18 TEM characterization of AuNPs. (a) TEM image of 12.5 nm AuNPs with 50 nm scale bar. (b) TEM image of 12.5 nm AuNPs with 50 nm scale bar

2.6 Characterization of AuNCs

Unlike the UV-vis absorption spectra of large Au nanoparticles that shows a strong peak at around 520 nm, UV-vis absorption spectrum of AuNCs display two weak peaks at around 505 nm and 560 nm which arises from mixed interband (sp to sp) and interbands (d to sp) [36]. The absorption of AuNCs under UV-vis light is presented in Fig. 19 (a). Additionally, AuNCs luminesce bright red under UV excitation (Fig. 19 (b)). This behavior of AuNCs is caused by interband transition between 5d and 6sp [67, 68]. Also, TEM was used to indicate morphology and the core size of AuNCs. Fig. 20 shows the size of 2 nm of the sample by TEM imaging. The concentration of AuNCs assumed to be a little smaller than the amount of gold used in the synthesis process. Thus, the AuNCs concentration is about 20 mg/ml.
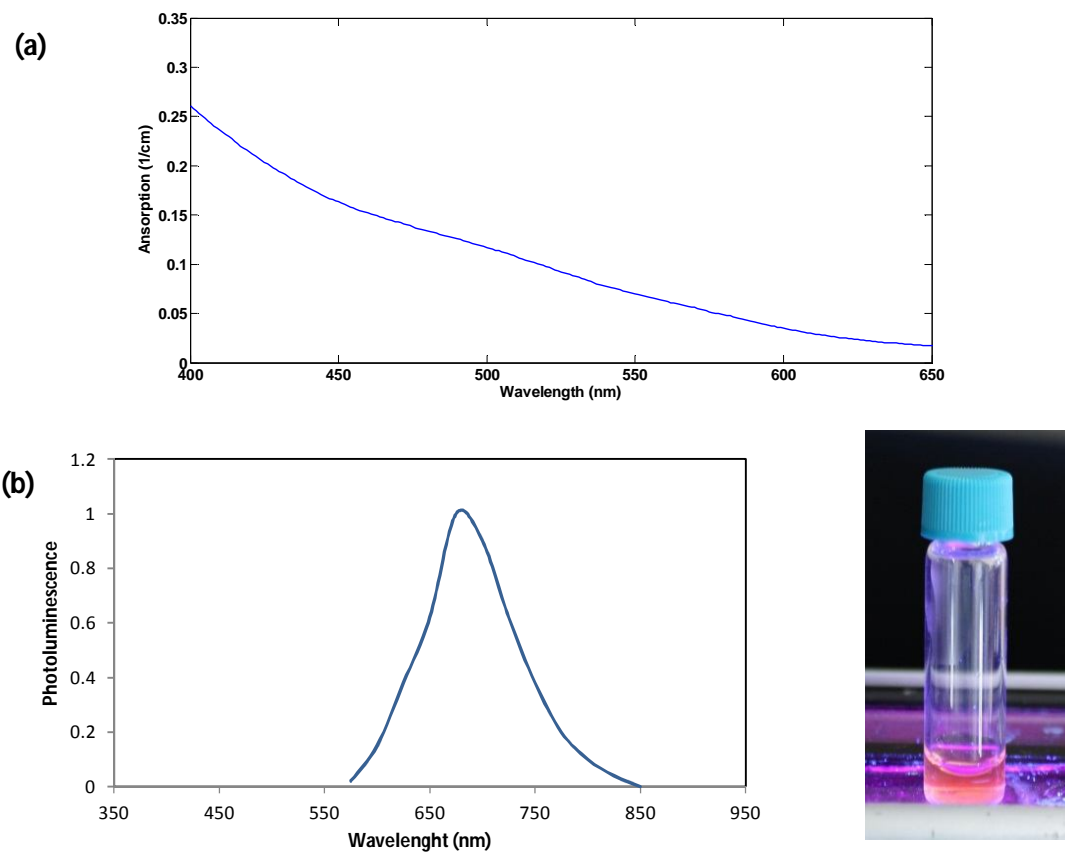
Fig. 19 Characterization of AuNCs. (a) UV-vis spectroscopy of AuNCs. (b) Left: Emission Spectrum of AuNCs. Right: Luminescent emission of AuNCs under UV light.
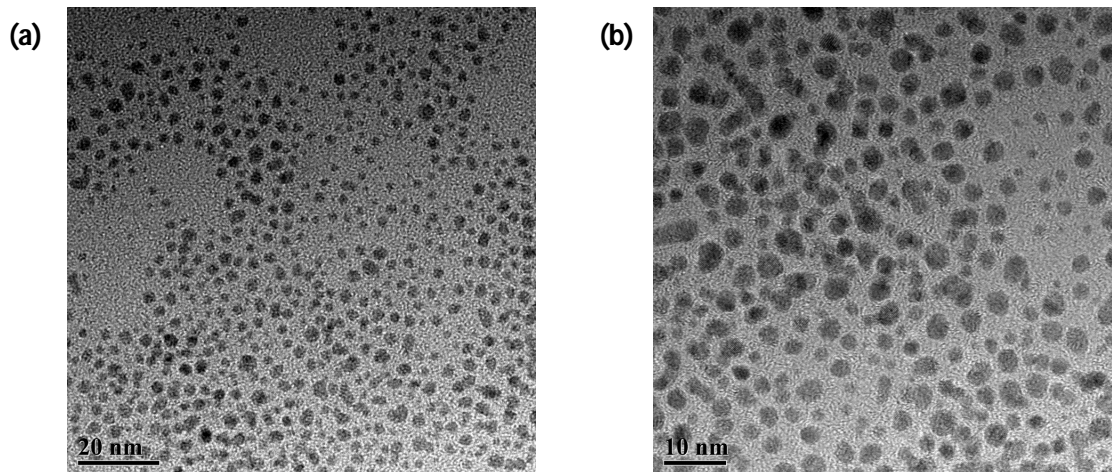
Fig. 20 TEM images of 1.7 nm AuNCs. (a) With 20 nm size scale. (b) With 10 nm size scale.

CHAPTER III

EXPERIMENTAL TESTS OF NANOPARTICLES

3.1 Microwave Test of Nanoparticles

As mentioned earlier, illumination of nanoparticles at the proper wavelength (energy) can locally deposit heat. By adjusting the microwave frequency, the penetration depth will be varied. For example, 3 GHz wave can penetrate 9 cm into fat and 1.2 cm into muscle but at 300 MHz source, the wave penetrates 30 cm into fat and 4 cm into muscle [74]. To elucidate the physical mechanism of heat generation by nanoparticles, resuspended nanoparticles in DI-water were exposed to microwave energy at fixed pulse frequency of 3 GHz. For this purpose, nanoparticles solutions were placed in CEM Discover Microwave system which uniformly propagated electromagnetic field through the sample and greatly reduced reaction time. By placing the sample at the middle of the microwave generator, the sample can be irradiated constantly with microwave energy (Fig. 21). To systematically study the heat generation in metal and magnetic nanoparticles by microwave energy, different weight percent concentrations of each sample were tested at the same condition during one minute with the same amount of volume of 0.5 ml. All nanoparticle heating profiles were compared to the heating profile of DI-water tested in the same conditions. Water content in biological samples poses an obstacle, as it is the primary absorber of microwave radiation in the body. Thus, the thermal production of nanoparticles as a hyperthermic or contrast agent must exceed that of water.
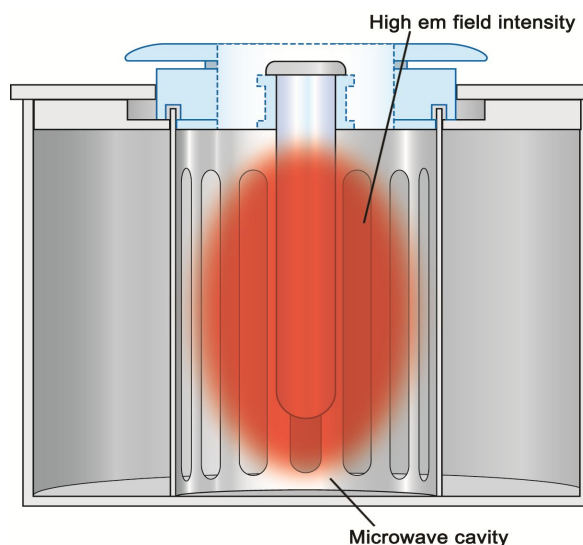
Fig. 21 Illustration courtesy of CEM Corporation © 2006 [75].

3.1.1 SPION Heat Generation Under 3 GHz

In the synthesis process of SPIONs described in the section 2.1, the surface functionalization of SPIONs was provided by citric acid (CA). CA has the potential for the ionic conductivity and may effect in the heat generation via microwave irradiation. Thus, the SPIONs solution was subjected to dialysis after synthesis. To study precisely the effect of CA in heat deposition by SPIONs under microwave energy, the SPIONs were dialyzed for four different time duration: 24 hours, 48 hours, 72 hours, and 96 hours. In each time step, a portion of sample was centrifuged at 1200 rpm for 15 minutes to separate the nanoparticles from the background solution containing CA. Then the pellet part was re-suspended into DI-water (Fig. 12 (b)) in a way to get different concentrations of SPIONs including 0.68, 1.37, 2.75, 5.5, 11,22, and 44 mg/ml, respectively. Then, the 0.5 ml of stock solution (before centrifugation with initial concentration), supernatant and SPIONs with different concentrations were exposed to microwave energy at 3 GHz for one minute. Fig. 22 shows the thermal behavior of SPIONs at different dialysis times. After 24 hours dialysis, the final temperature of the

35

stock solution and supernatant, denoted by ST and SN in the figure, respectively, is much higher than the initial concentration of SPIONs (11 mg/ml). This fact indicates that there were significant amount of CA remained in the stock solution and supernatant after 24 hours dialysis, which causes the ionic conductivity and thus, increase the temperature of stock solution and supernatant to 58º C to 57º C, respectively. The stock solution consist a little higher amount of CA in comparison with supernatant due to centrifugation of the SPIONs solution and remaining a small portion of CA in pellet part. As shown in Fig. 22 (a) even very high concentration of SPIONs (44 mg/ml) do not enhance the temperature as high as stock solution and supernatant. In Fig. 22 (b), after 48 hours dialysis, the stock solution and supernatant raise the temperature up to 57º C and 51º C, respectively. The one degree degradation of the stock solution temperature after 48 hours compared to 24 hours, reveals lower amount of CA in solution due to extra dialysis time. After 72 hours dialysis, the final temperature enhancement of stock solution and supernatant part drop to 55º C and 53º C, respectively (Fig. 22 (c)). Finally, after 96 hours dialysis, the temperature of stock solution and supernatant part enhance 41º C and 40º C, respectively. At this step the temperature increase of both stock solution and supernatant part are below SPIONs with initial concentration (the pellet part resuspended into DI-water after 96 hours dialysis) during one minute. This fact proves that there is negligible amount of CA in the SPOIN solution after 96 hours and it does not result in heat generation under microwave energy. At this time step, we stop dialyzing SPIONs solution. After that, different concentration of SPIONs were placed into microwave generator and irradiated by microwave energy at 3 GHz for one minute. The results shown in Fig.19.d indicate that high concentrations of SPIONs (44 mg/ml) are able to convert microwave energy into heat and enhance the temperature up to 48 º C. The temperature difference between highly concentrated SPIONs compared to DI-water is 22 º C.
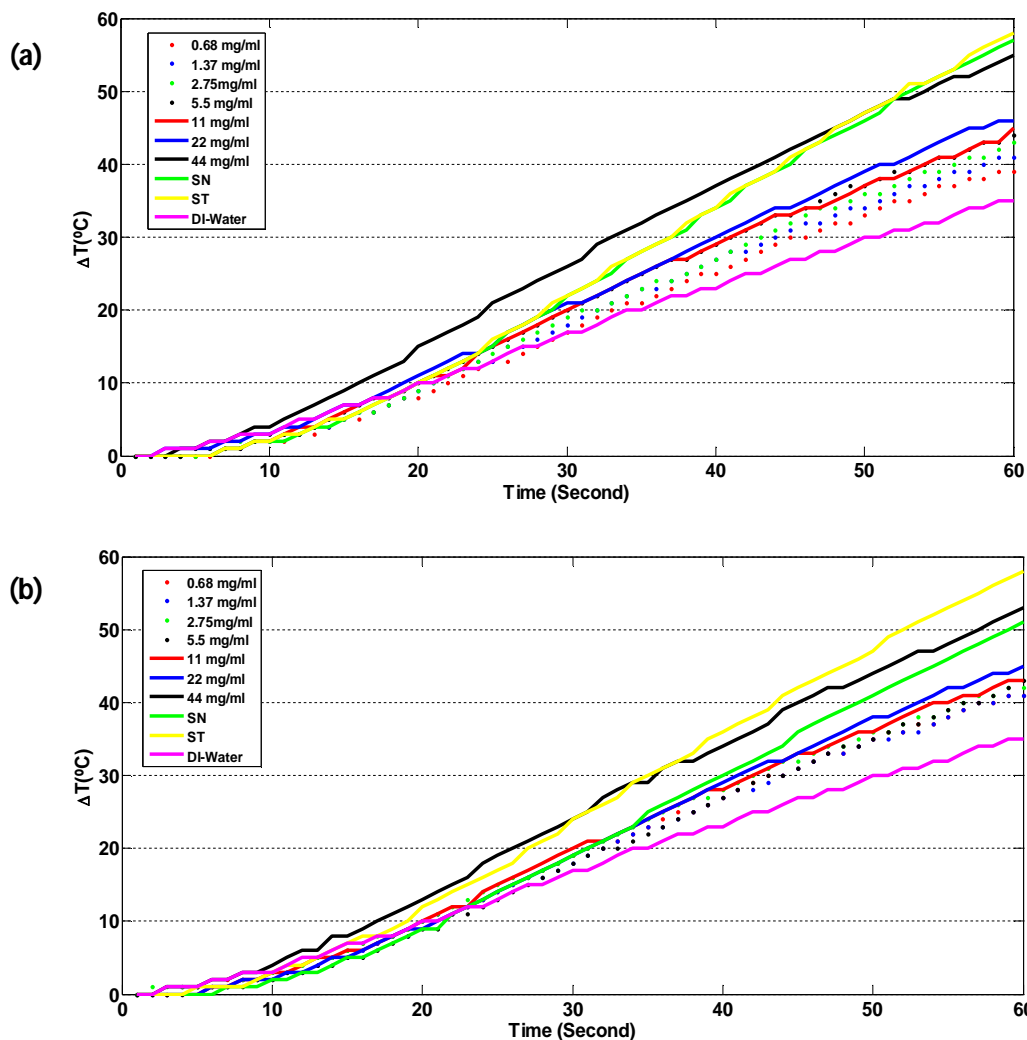
Fig. 22 Thermal behavior of SPIONs solution after 60 seconds under 3 GHz energ. (a) Thermal behavior of SPIONs after 24 hours dialysis. (b) Thermal behavior of SPIONs after 48 hours dialysis. (c) Thermal behavior of SPIONs after 72 hours dialysis. (d) Thermal behavior of SPIONs after 96 hours dialysis reflects low citric acid level.
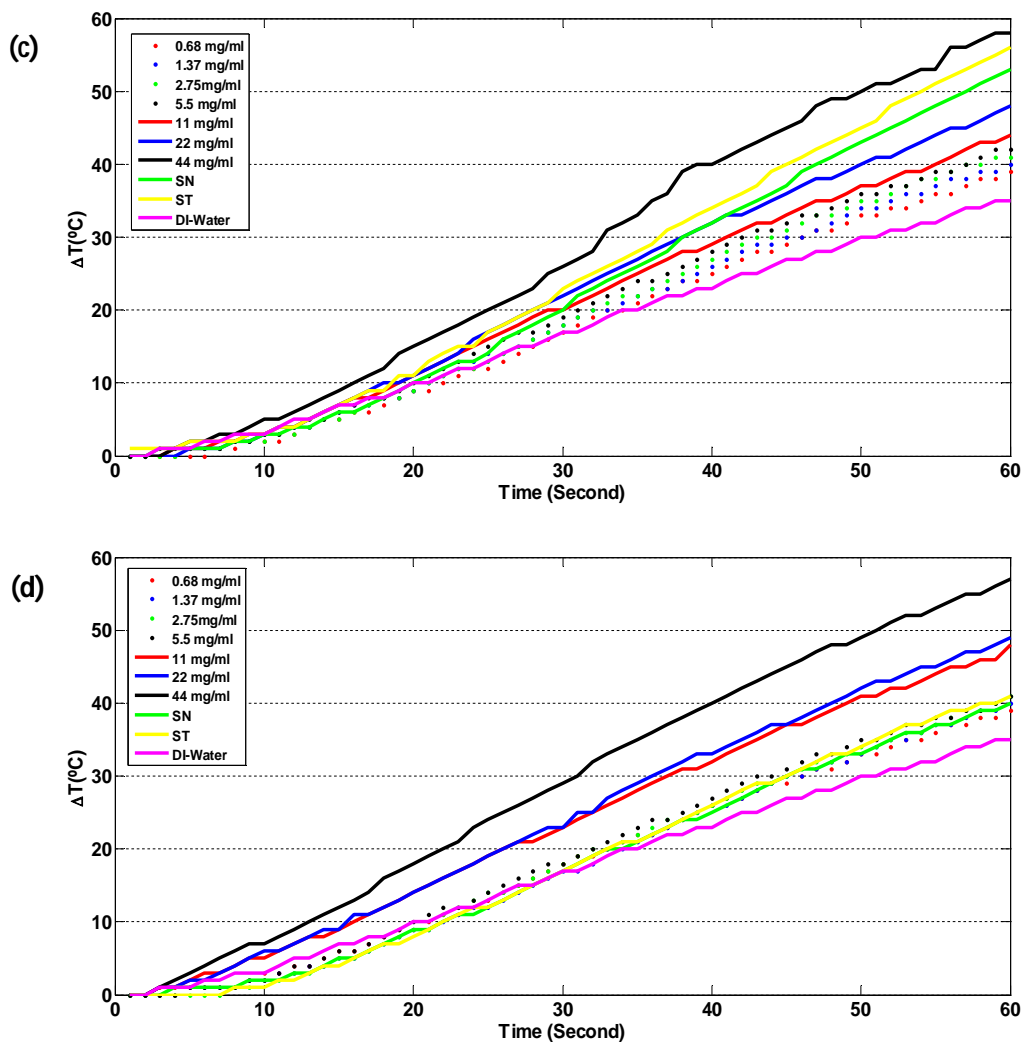
Fig. 22 Continued.

3.1.2 AuNPs Heat Generation Under 3 GHz

To be able to determine the role of AuNPs in heat generation, the colloidal solutions were centrifuged at 12,000 rpm for 15 minutes. The supernatant was decanted and the pellet was resuspended in DI-water in a way to end up with one, two, and four times concentrated of AuNPs compared to initial concentration. Then supernatant solution and resuspended AuNPs solutions with different concentrations were separately

characterized by UV-vis spectroscopy. All the AuNPs solutions revealed SPR peak around 520 nm, while supernatant solution had absorption spectra similar to DI-water. After that, DI-water, stock solution, and AuNPs solutions with different concentrations were subjected to CEM microwave system at same conditions equal to 30 W power and same volumes equal to 0.5 ml for one minute. Fig. 23 shows the thermal behavior of AuNPs solution under microwave energy at 3GHz recorded by CEM. The thermal trend of AuNPs solution with initial concentration (0.2 mg/ml) under microwave energy is very close to DI-water that indicates that 0.2 mg/ml AuNPs cannot transfer microwave energy into heat higher than water. Interestingly, three other prepared samples with higher concentration (0.4 mg/ml and 0.8 mg/ml, and 2.4 mg/ml) have very similar thermal behavior that end up only 3° C higher than DI-water after one minute. It should be noted that the high concentration of AuNPs is still significantly lower than the initial concentration of SPIONs; in this experiment, we tried to concentrate the AuNPs solution by centrifugation to as high a level as possible (twelve times concentrated AuNPs which corresponds to 2.4 mg/ml) to study the role of AuNPs in heat generation. The limitations of using a larger amount gold salt in the synthesis process are that it increases the AuNPs diameter. Based on this experiment, it can be concluded that AuNPs do not efficiently transduce microwave energy into thermal energy. On the other hand, stock solution and supernatant have very similar temperature trends after exposure to microwave energy and result in a temperature rise that is 17 °C higher than DI-water. This fact reveals that the presence of citrate used in the synthesis process of AuNPs to stabilize nanoparticles from aggregation yields ionic conductivity and thus, citrate is responsible for noticeable heat generation in both stock solution and supernatant. The temperature enhancement of AuNPs solution reported before [12] is due to ions (e.g. citrate) in the aqueous solution of AuNPs.
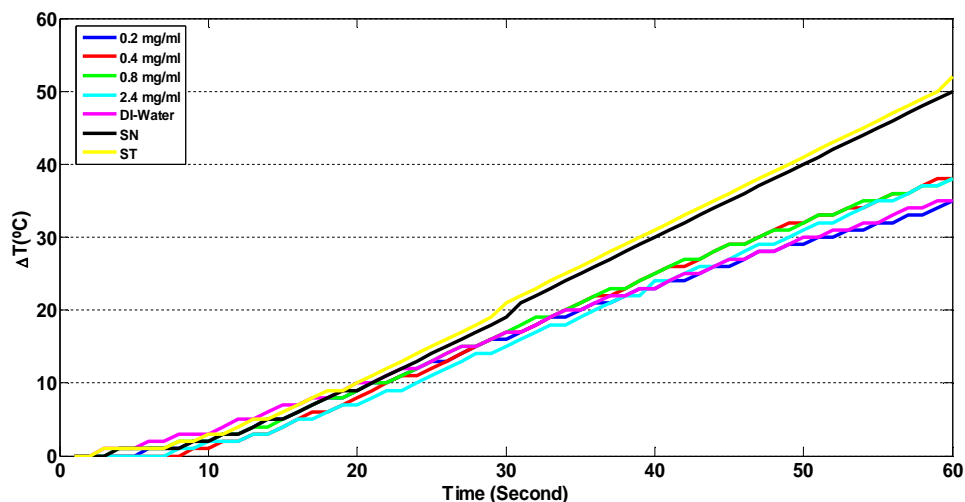
Fig. 23 Thermal behavior of AuNPs solution after 60 seconds under 3 GHz energy. Negligible temperature enhancement of concentrated AuNPs reveals that AuNPs do not contribute to microwave absorption to thermal conversion.

3.1.3 AuNCs Heat Generation Under 3 GHz

AuNCs were purified after synthesis by triple centrifugation at 1100 rpm for 30 minutes using filters with molecular weight cut-off 10 kDa. The pellet was resuspended in DI-water to yield concentrations of 10 mg/ml, 20 mg/ml, and 40 mg/ml, corresponding to $\times \frac{1}{2}, \times 1, \times 2$ of initial concentration, respectively. Then 0.5 ml of each sample was placed in the microwave generator (CEM) at 30 W power and after one minute the thermal trend of each was recorded. Fig. 24 represents the temperature rise of AuNCs with different concentrations and DI-water. The two lower concentrations of AuNCs solutions, 10 mg/ml and 20 mg/ml, heat up to $40°$ C and $41°$ C, which is $5°$C and $6°$ C higher than DI-water temperature enhancement, respectively. By increasing the concentration of AuNCs in the solution to 60 mg/ml, the temperature change increases to $44°$ C. This temperature is $9°$C higher than the DI-water temperature change during one minute under the same conditions. In contrast to the AuNPs solutions which were not able to transfer microwave energy into heat (section 3.1.2), AuNCs are capable of enhancing

temperature by exposing to microwave energy at 3GHz. This property of the AuNCs solution arises from supra-molecular properties of AuNCs. The microwave energy absorbed between sub-conduction bands 5d and 6sp which cause the conversion of microwave energy into heat in a non-radiative process.
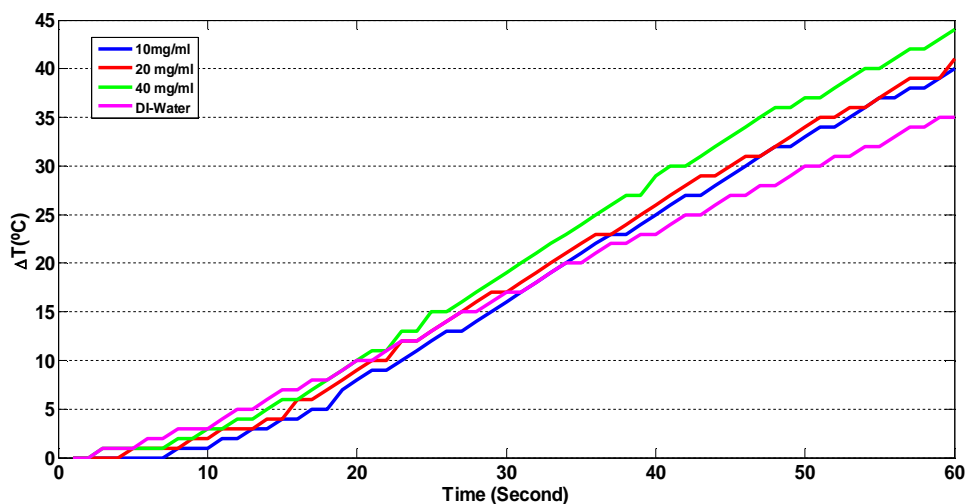
Fig. 24 Thermal behavior of AuNCs solution after 60 seconds under 3 GHz energy. The plot shows that high concentrations of AuNcs are able to transfer microwave into heat up to 9°C compared to DI-water.

3.2 Complex Permittivity Measurements of Nanoparticles

The microwave test of nanoparticles provides quantitative measurement, but still more detail is needed for analyzing the microwave properties of nanoparticles. The ratio of permittivity of a material to that in vacuum (dielectric constant) determines the microwave absorption at different frequencies. Thus, in this study, the absorption spectrums of nanoparticles were calculated by measuring their complex permittivities. In our experiment, a dielectric dip probe kit has been chosen for measuring complex permittivity as it is ideal for liquid and semi-solid materials [9]. The system includes a

41

coaxial dip probe kit, a vector network analyzer and a radiofrequency source. We used the Agilent 85070E Dielectric Probe Kit which consists of a stainless steel tube with a conducting wire through the center. The nanoparticle solution fills the tube and serves as the dielectric. We also used Agilent E8364C PNA Network Analyzer to make broadband measurement from 500MHz to 10GHz. In this study, the complex permittivity of nanoparticles was measured by Air Force Research Laboratory (AFRL). Fig. 25 shows the schematic graph of the experimental set up for measuring dielectric properties. The dielectric properties of nanoparticles are measured by immersion the probe in the enough of nanoparticles solution (25 ml) to appear infinite to the probe. The experiment yields the real and imaginary parts of the dielectric properties. The open ended probe propagates electric field into the samples and the relative permittivity of the nanoparticle sample measure. It has to be mentioned that the calibration of the system must be performed before each measurement by using the difference between actual and predicted values of three well-known standard samples to remove repeatable errors [9]. It is also important to make sure that the cable is fixed and not bent between calibration and measurements. The bubbles on the tip of the probe must be carefully removed to reduce the effect of air in the measurements.
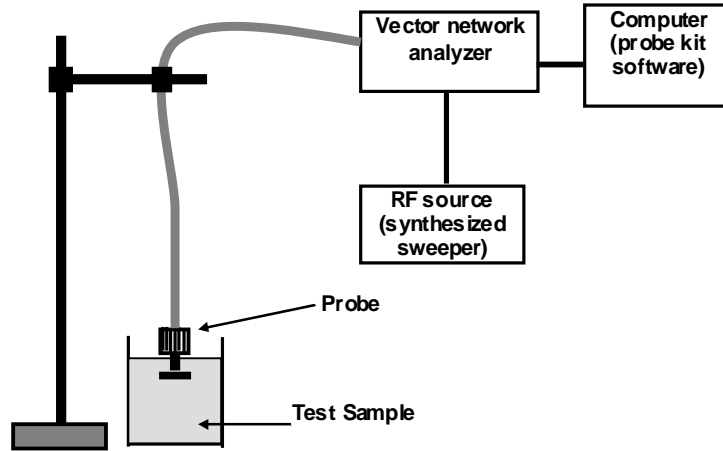
Fig. 25 Schematic set up for measuring dielectric properties [9].

3.3 Calculation of Nanoparticles Absorption Coefficient

In this study, the complex permittivities of the three different aforementioned nanoparticles were measured with the method described in previous section to identify the absorption of nanoparticles in the microwave spectrum. The complex relative permittivity $\varepsilon^{''}(\omega)$ was represented as $\varepsilon^*(\omega) = \varepsilon_r(\omega) - j\varepsilon_i(\omega)$ where ε_r and ε_i are the real and imaginary parts of the complex relative permittivity, respectively. For all three nanoparticles, the real part of complex permittivity drops by increasing frequency while the imaginary part rises with increasing frequency. As Fig. 26 (a) shows, the real component of SPIONs drops by increasing concentration of nanoparticles and DI-water has the highest real part of complex permittivity. On the contrary, the imaginary part of SPIONs rises up by increasing concentration of nanoparticles and DI-water has the lowest imaginary component compared to all different concentration of SPIONs (Fig. 26 (b)). The real part of complex permittivity of AuNPs has a completely different behavior with SPIONs and degrades by decreasing concentration (Fig. 27 (a)). AuNPs with different concentrations have dissimilar trend at two distinct frequency rang. From 500

43

MHz to 800 MHz, 0.2 mg/ml AuNPs, has the highest imaginary component, while in the range between 800 MHz and 10 GHz this value decreases in a way that DI-water reaches the highest imaginary part (Fig. 27 (b)). Real part of complex permittivity of AuNCs trends similarly to SPIONs which fall down by diluting the sample (Fig. 28 (a)). The imaginary part of complex permittivity of AuNCs degrades by decreasing concentration and DI-water has the largest imaginary part of complex permittivity (Fig. 28 (b)).
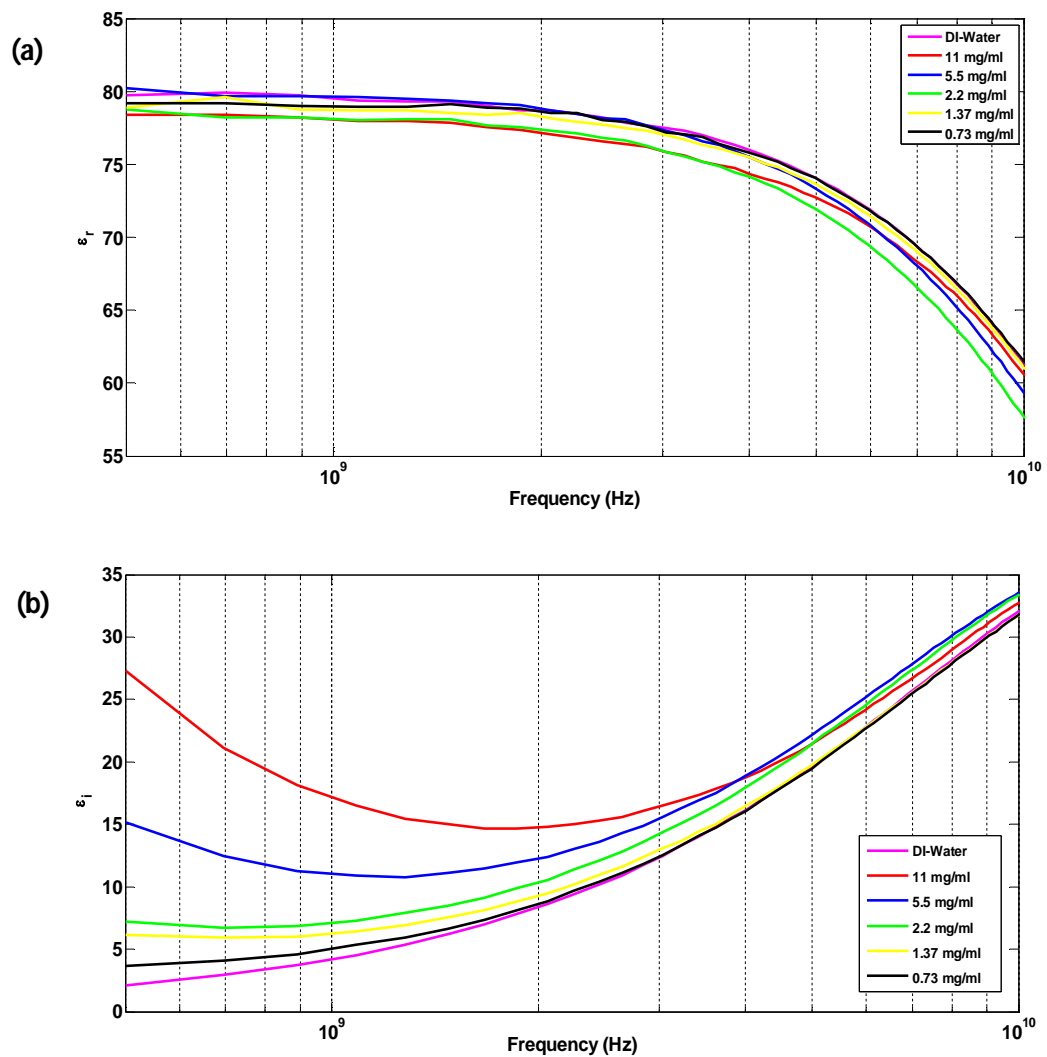
Fig. 26 Dielectric properties of SPIONs. (b)Real parts. (b)imaginary parts.
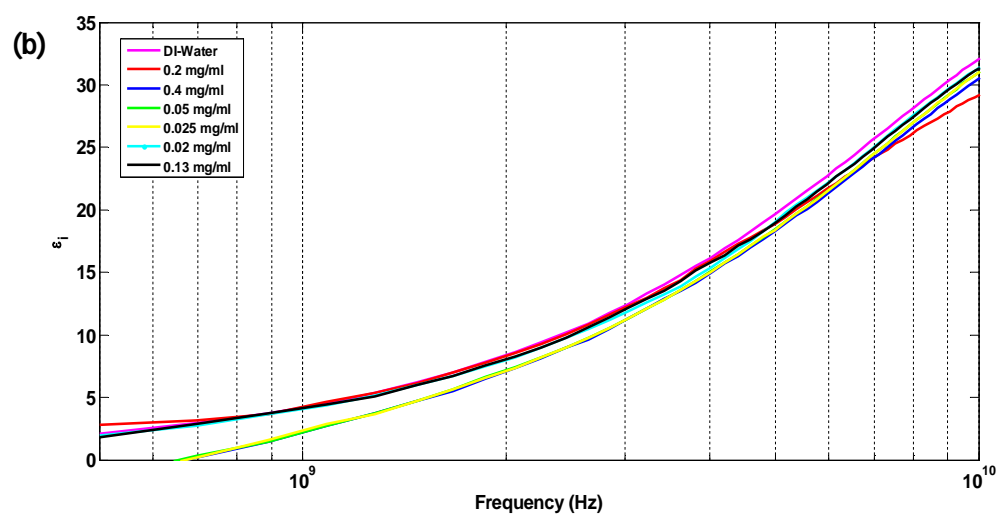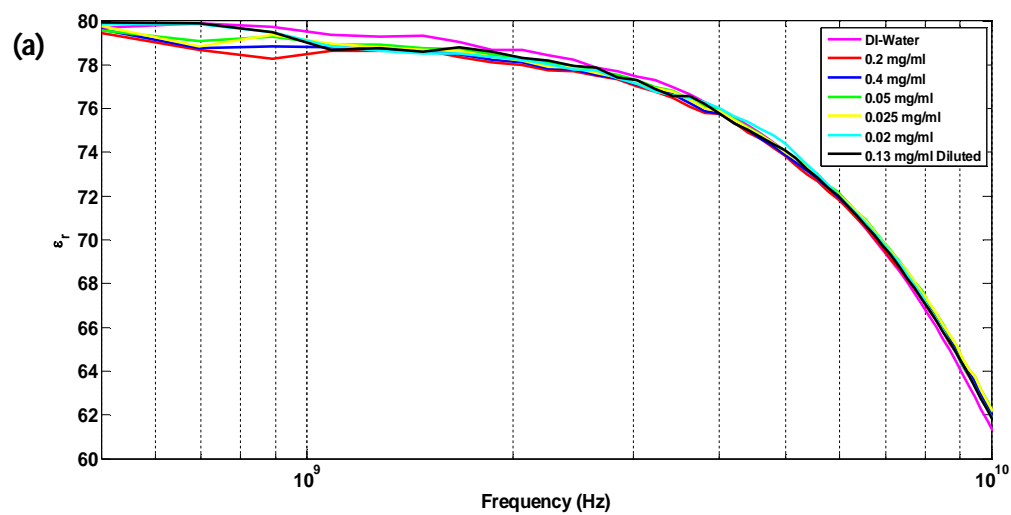
Fig. 27 Dielectric properties of AuNPs. (b) Real parts. (b) imaginary parts

45
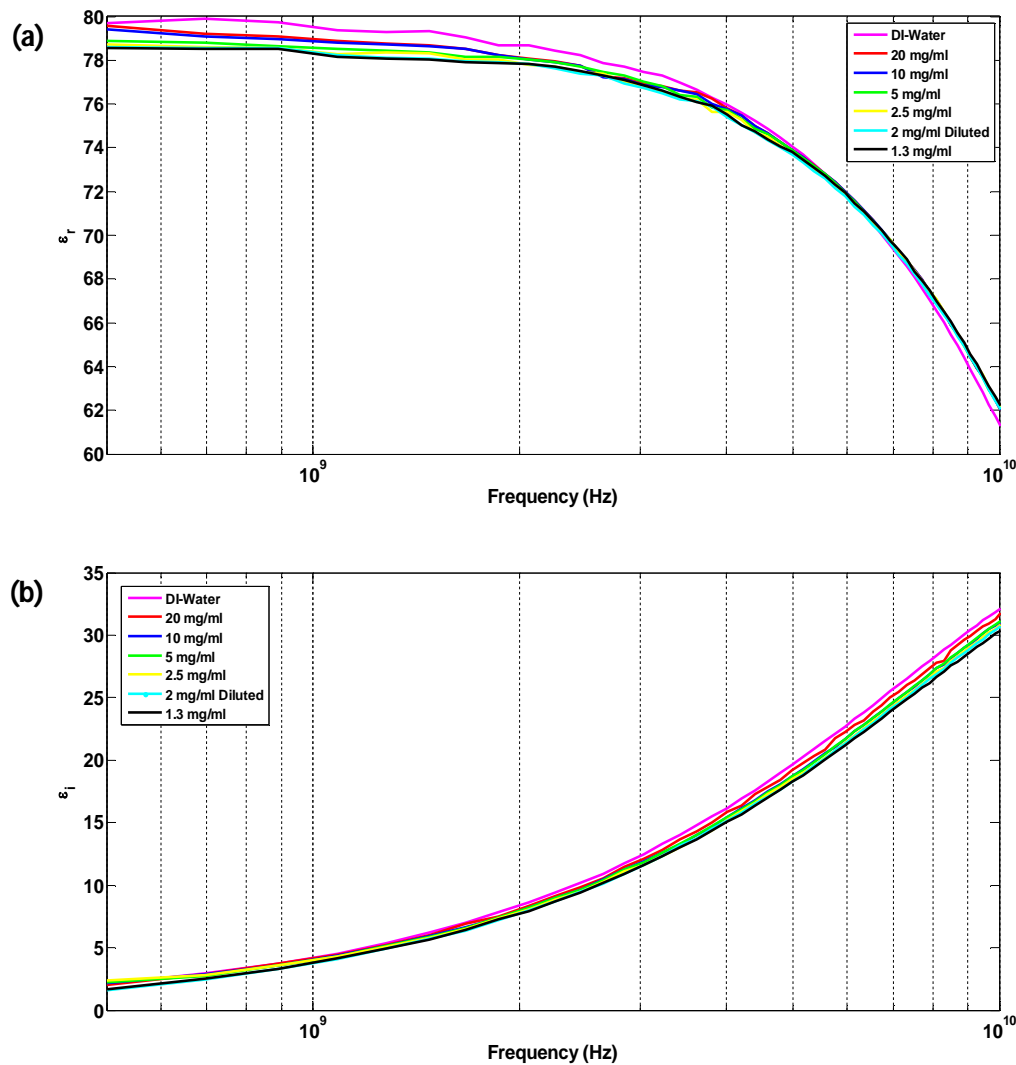
Fig. 28 Dielectric properties of AuNCs. (b)Real parts. (b)imaginary parts.

Two different definitions of complex refractive index can be used to derive absorption coefficient. The first definition is the square root of the product of the complex relative permittivity and complex relative permeability as presented in Eq. (6), and the second is derived from extinction coefficient as shown in Eq. (7):

$$n^*(\omega) = \sqrt{\varepsilon(\omega)\mu(\omega)} \tag{6}$$

$$n^*(\omega) = n(\omega) - jk(\omega) \tag{7}$$

where $n(\omega)$ is the refractive index as a function of the frequency of light and $k(\omega)$ is the extinction coefficient which is equal to $k(\omega) = \lambda\alpha(\omega)/(2\pi)$. From simple derivation, the microwave absorption coefficient of a material can be obtained as:

$$\alpha(\omega) = \frac{\omega}{c_0}\sqrt{\frac{\mu_r(\omega)\varepsilon_r(\omega)}{2}\left(\sqrt{1 + \left(\frac{\sigma(\omega)}{\omega\varepsilon_0\varepsilon_r(\omega)}\right)^2} - 1\right)} \tag{8}$$

In Eq. (8), $\mu_r(\omega)$ is real component of the relative complex permeability at angular frequency and obtained from dip probe kit, c_0 is the speed of electromagnetic waves in vacuum (approximately 3×10^8 m/s), and $\sigma(\omega)$ is the conductivity which is defined as $\omega\varepsilon_0\varepsilon_i(\omega)$ ($\varepsilon_0 = 8.85\times10^{-12}$ F/m) [9]. It should be pointed out that the conductivity of the nanoparticles is related to imaginary component of its complex permittivity. SPIONs, which show a big difference in ε_i between different concentrations and DI-water, are expected to have significant absorption coefficients. Oppositely, the ε_i for both AuNPs and AuNCs are very similar for different concentration and DI-water. Thus, the absorption coefficients at different concentrations are expected to be close to that of DI-water. Using the complex permittivity and Eq. (8), the absorption spectrum of SPIONs, AuNPs, and AuNCs were calculated and shown in Fig. 29. As expected, SPIONs show microwave absorption above DI-water and the absorption increases with increasing nanoparticle concentration. The microwave absorption of 11 mg/ml SPIONs is approximately 20 1/m larger than DI-water (Fig. 29 (a)). Conversely, AuNPs absorption drops with increasing concentration and interestingly, DI-water has the highest absorption rate compared to all concentrations of AuNPs (Fig. 29 (b)). AuNC absorption

spectrum is still lower than DI-water but the absorption rate degrades by diluting AuNCs solution (Fig. 29 (c)). This difference in AuNPs and AuNCs may arise from the sub-conduction band transition of AuNCs. Fig. 30 reveals the absorption rate of SPIONs, AuNPs, and AuNCs with initial concentrations and DI- water.
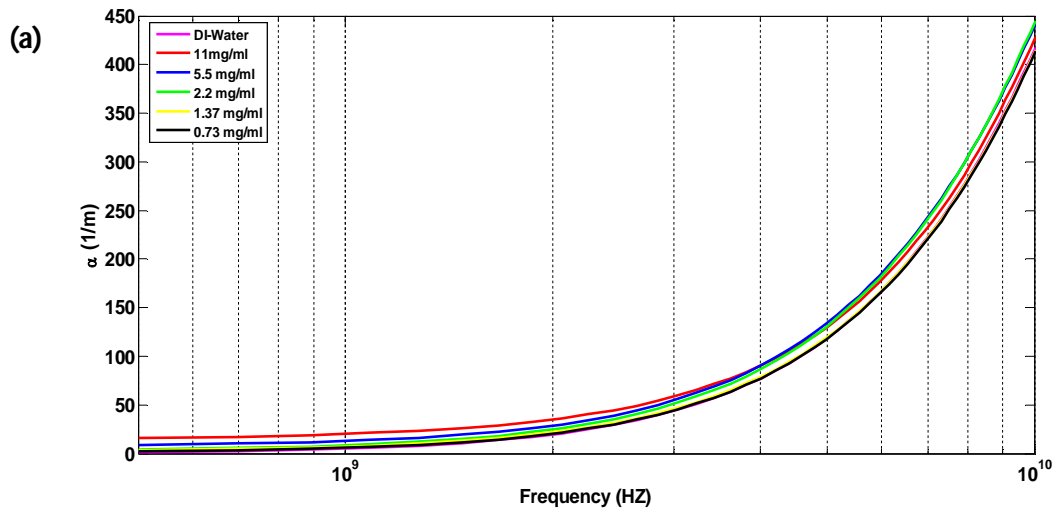

Fig. 29 Absorption spectrums of nanoparticles. (a) SPION absorption spectrum. (b) AuNPs absorption spectrum (c) AuNCs absorption spectrum.
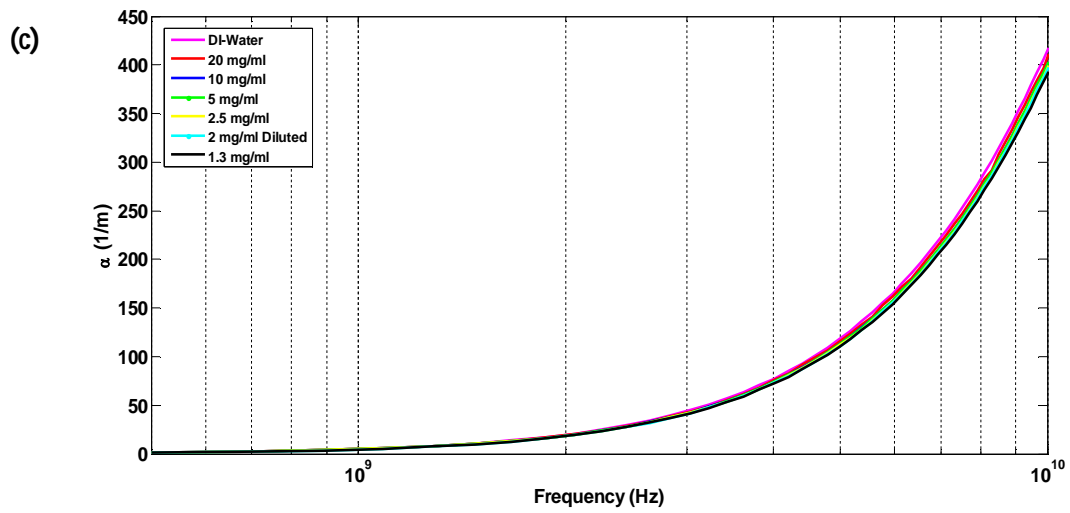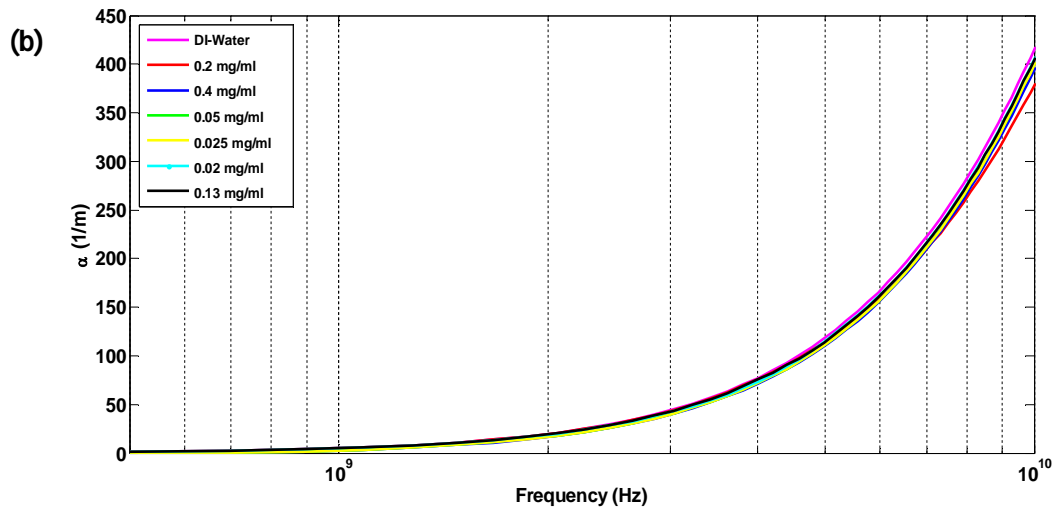
Fig. 29 Continued.
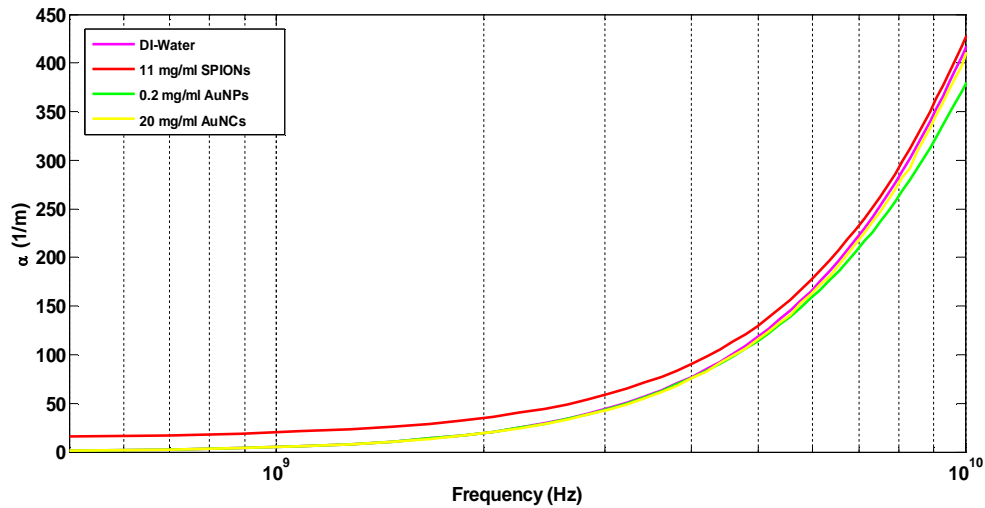
Fig. 30 Absorption spectrum of DI-water, SPIONs, AuNPs, AND AuNCs with initial concentrations.

3.4 Nanoparticles Signal Responses and TAT Imaging

3.4.1 Material and Method

As described in section earlier, water is the main absorber of microwave energy in the biological samples. This water absorption enables thermoelastic expansion of the sample, when it is exposed to microwave energy in TAT system. However, using water, alone, limits this technique. The contrast obtained by water may not be high enough for identification of desired items in the sample. Also, water limits the penetration depth. Addition of exogenous contrast agents that absorbs microwave energy greater than water, cause the observation of the features in the sample that may otherwise be unseen. In this study, all aforementioned nanoparticles with different concentrations were tested as exogenous contrast agents in a TAT system in Dr. Wang's lab in Washington University.
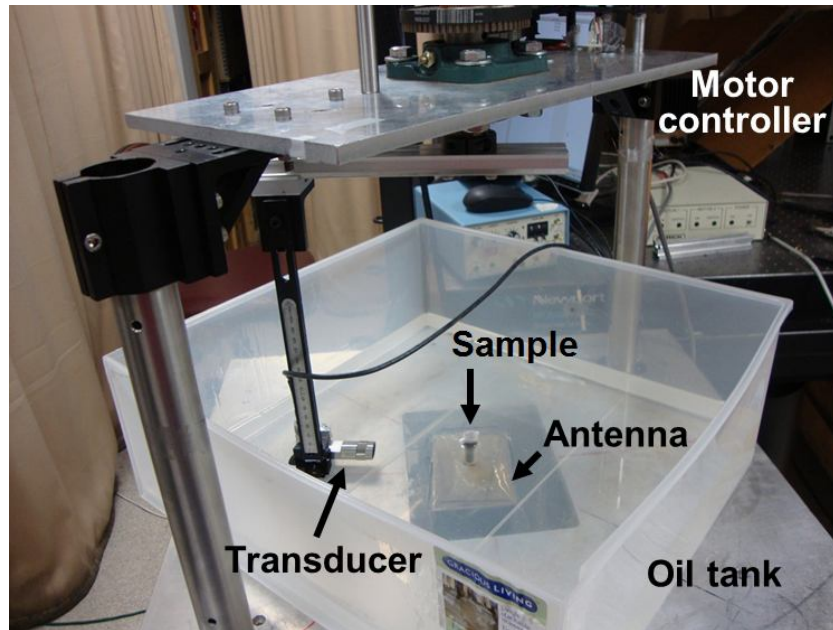
Fig. 31 Experimental set up of TAT imaging system.

Fig. 31 shows the system set up of TAT system used in this study. The microwave generator produces 3.0 GHz pulses with different pulse width from 0.16μs to 1.2 μs and repetition rate lower than 100 Hz. For this experiment, the microwave pulse width was 0.05 μs and sampling rate was 20 MHz .The custom made data acquisition controlled the triggering and collected the raw data for post-processing and image reconstruction. For each nanoparticle sample, the data was collected by transducer at 200 different positions over 180 degrees and the cross-sectional TAT images were reconstructed by Fourier beam-forming algorithm run in Matlab program [76]. To improve signal to noise ratio (SNR), TA acquisitions were repeated 68 times and raw data were averaged before post-processing and image display.

3.4.2 TAT Results and Discussion

Low-density polyethylene (lDPE) tubes filled with the Nanoparticles solution with different concentrations and were embedded in a mineral oil tank. The reason is that mineral oil has very small microwave absorption, thus maximum energy will reach the sample. The diameter of the tube was 13 mm. The location of the tube was kept at approximately the same position for each experiment. Each tube filled with the sample was identified by the boundaries facing the transducer. Because the low frequencies were filtered by the ultrasound transducer, only the boundaries are detectable. In addition, the transducer position was fixed, and hence the boundaries at some positions were not detected. In this study, we started filling the LDPE tube with the lowest concentration of SPIONs solution and then gradually increased the concentration. After running each experiment, the tube was carefully cleaned to reduce the influence of remaining particles in the next measurement. Then, the LDPE tube was completely replaced with a new one to be filled with AuNPs solution. This process was repeated for testing AuNCs solution as well. Since the position of the tube might be changed after replacing with a new tube, DI-water measurement was repeated after each two replacement of tubes. Irradiating microwave energy at fixe pulse frequency of 3 GHz to the samples, the time-resolved thermoacoustic signal of the samples were measured and compared to that of DI-water. Based on the TAT concept, the greater microwave absorption by the contrast agents is identified by an increase in the peak value of the produced TA signal. Subsequently, the larger peak value of TA signal defines higher TAT image contras.
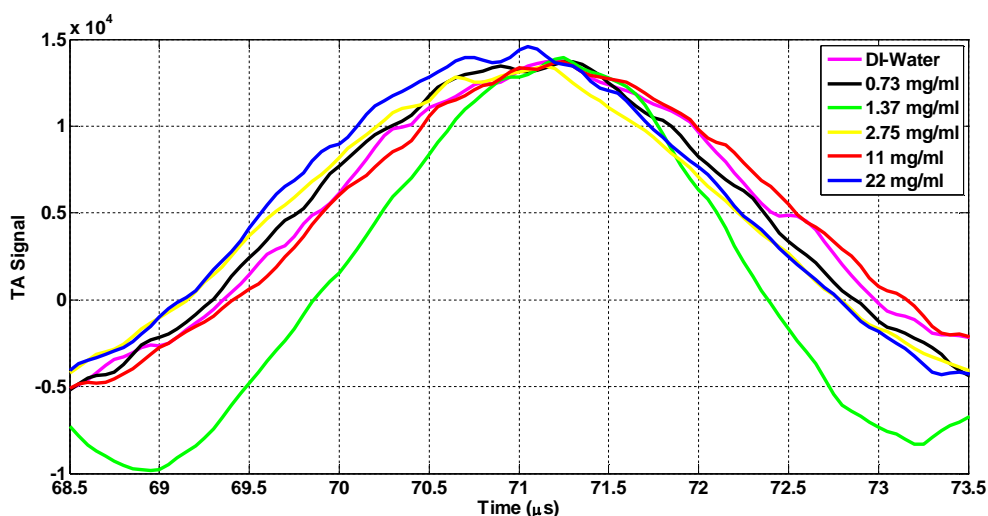
Fig. 32 Time resolves thermoacoustic signal of SPIONs.

After running TAT experiment at 200 different positions for each sample, the signal with highest peak value was plotted and compered with DI-water. Fig. 32 shows the strength of DI-water signal and SPIONs with different concentrations. As was predicted by calculating absorption coefficient of SPIONs, higher concentrations of SPIONs (22 mg/ml) are able to absorb microwave energy greater than DI-water, and as a result have higher TA signal peak value compared to DI-water. All other concentrations of SPIONs absorb microwave energy slightly greater than DI-water (Fig. 29 (a)) and therefore the amplitude of their TA peak signal is very close to DI-water. This phenomenon was also estimated by microwave heating test of SPIONs via CEM. As described before, SPIONs are the only nanoparticles that transduce microwave energy into heat significantly. In another words, comparing these two properties of SPIONs (high microwave to thermal efficiency and high microwave absorption) with SPIONs, TA signal strength shows the consistent behavior for SPIONs. However, the thermal efficiency and microwave absorption of SPIONs are more significant, while there is just a very small increase in TA signal for high concentration SPIONs (22 mg/ml) compared to DI-water. This is due to the indirect measurement of TAT, which causes the energy lost throughout the process of converting microwave to thermoacoustic wave. The transduction of

53

microwave energy into heat by SPIONs is due to the magnetic dipole rotation in the presence of microwave field. Using all raw data at 200 positions over 180 degrees, the TAT image of each sample were reconstructed. Fig. 33 provides a quantitative view on the contrast increase by using 22 mg/ml SPIONs reconstructed from the TA signal. In this Figure, white arrows indicate the identification of the SPIONs tube's borders with higher contrast while the black arrows represent the reduction of contrast produced by DI-water in same positions. Fig. 34 illustrates that the reconstructed TAT images from lower concentration of SPIONs do not provide noticeable contrast compared to DI-water.
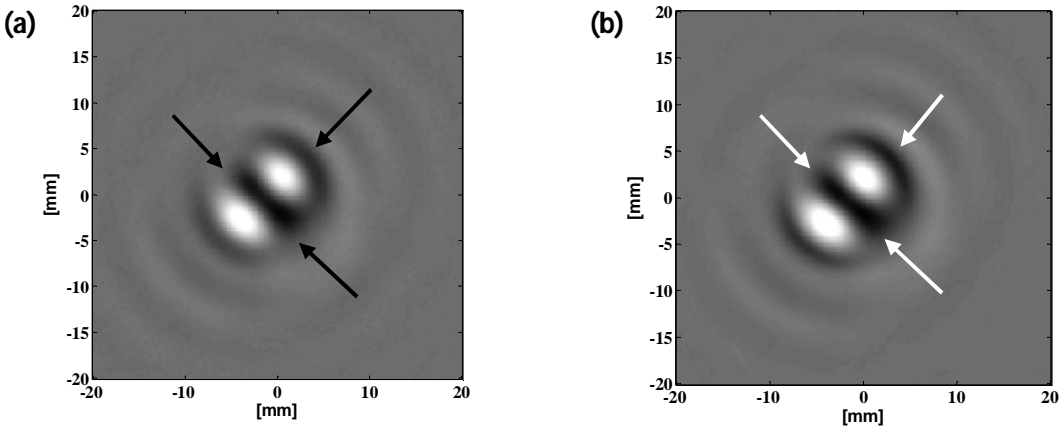
Fig. 33 TAT images of SPIONs. (a) DI-water. (b) 22 mg/ml SPIONs. The two bright spots inside the image are due to field distribution
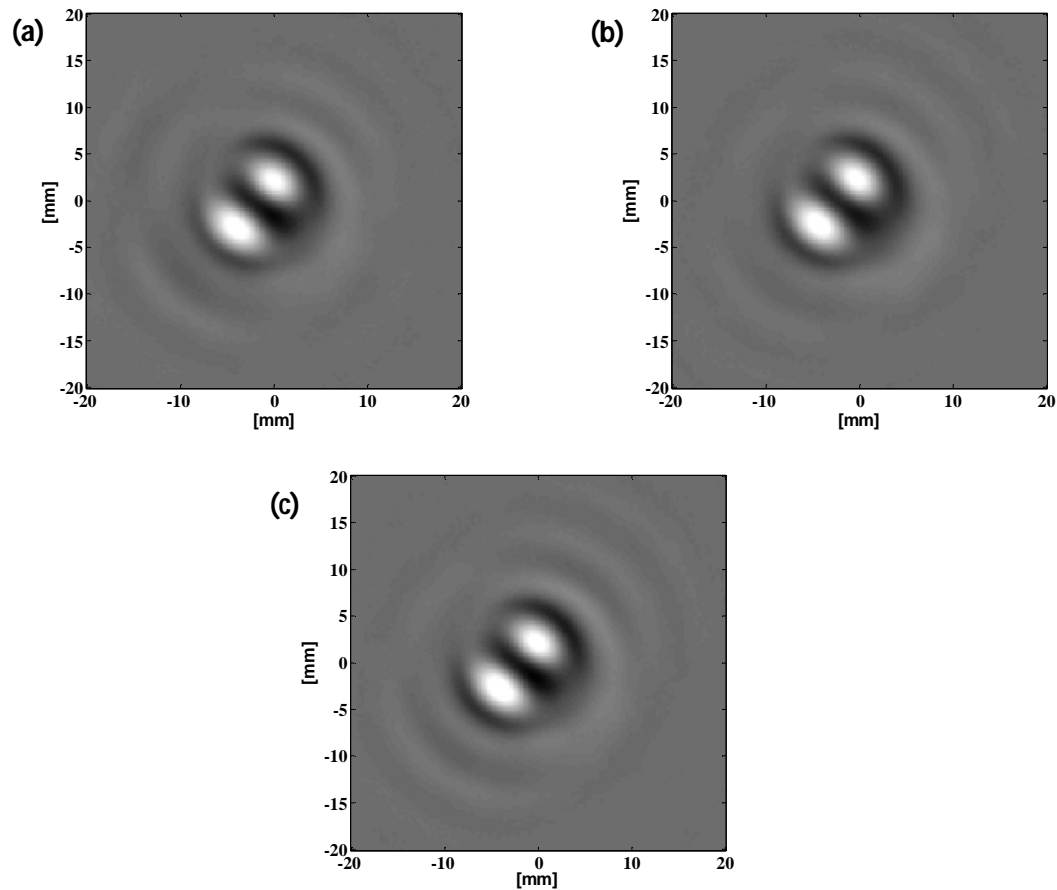
Fig. 34 TAT images of SPIONs. (a)11 mg/ml SPIONs. (b) 5.5 mg/ml SPIONs c) 0.275 mg/ml SPIONs

AuNPs has a dissimilar behavior in producing contrast compared to SPIONs. The time-resolve thermoacoustic signals of the AuNPs drop significantly by increasing concentration (Fig. 35). This trend was also seen in simulated absorption spectra of AuNPs described in the previous section. Additionally, low microwave absorption of AuNPs was foreseen by negligible AuNPs heat production under 3 GHz. This behavior implies the dilution of DI-water by AuNPs. In fact, by increasing AuNPs concentration we have less amount of DI-water to absorb microwave energy. Therefore, the absorption rate degrades by enhancing AuNPs concentration. Fig. 36 shows that the image contrast of the tube gradually degrades by increasing AuNPs concentration and DI-water provides the highest TAT image contrast compared to AuNPs solutions.

Fig. 35 Time resolved thermoacoustic signal of AuNPs
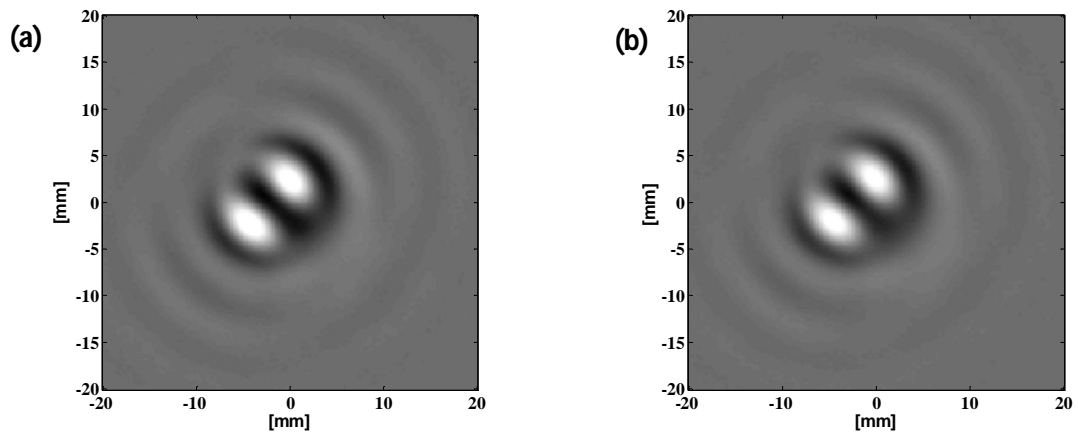
Fig. 36 TAT images of AuNPs. (a) DI-water. (b) 0.05 mg/ml AuNPs. (c) 0.1 mg/ml AuNPs. (d) 0.2 mg/ml AuNPs.
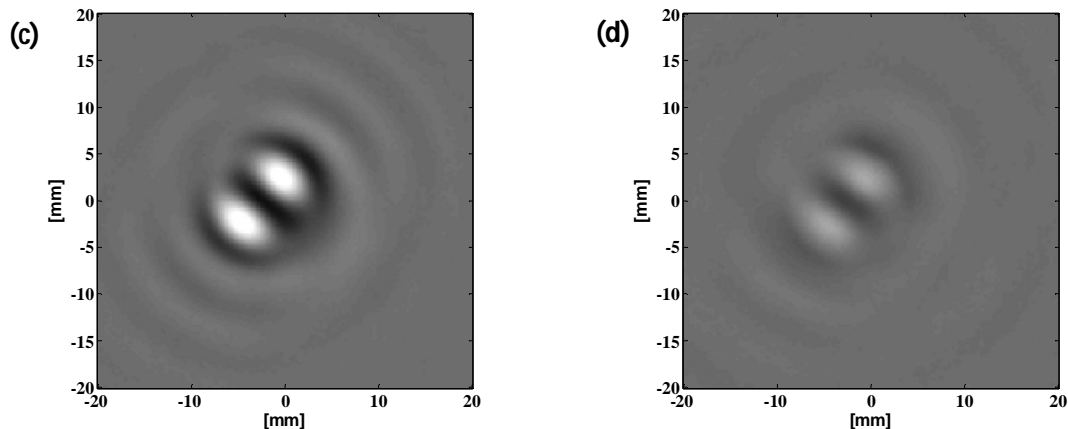
Fig. 36 Continued.

Testing AuNCs as contrast agent in the TAT system shows that they are not able to produce higher contrast than DI-water. Fig. 37 illustrates that the TA signal strength of AuNCs with different concentrations have lower amplitude than DI-water TA signals which are all very close at the peak value. Unlike to AuNPs, adding AuNCs to DI-water does not decrease the absorption spectrum of DI-water. This fact might be implying at the capability of AuNCs in absorbing microwave energy at very high concentration as was described in section 3.3. Consequently, the TAT images of all AuNCs solution and DI-water have the same contrast quality (Fig. 38). Moreover, only 4° C temperature enhancement of 20 mg/ml AuNCs compared to DI-water (described in section 3.1.3) indicates that they have low microwave absorption coefficient. However, the TA signal strength of AuNCs are lower than DI-water which is due to microwave energy lost in the process of changing microwave energy into thermoelastic wave in the TAT system.
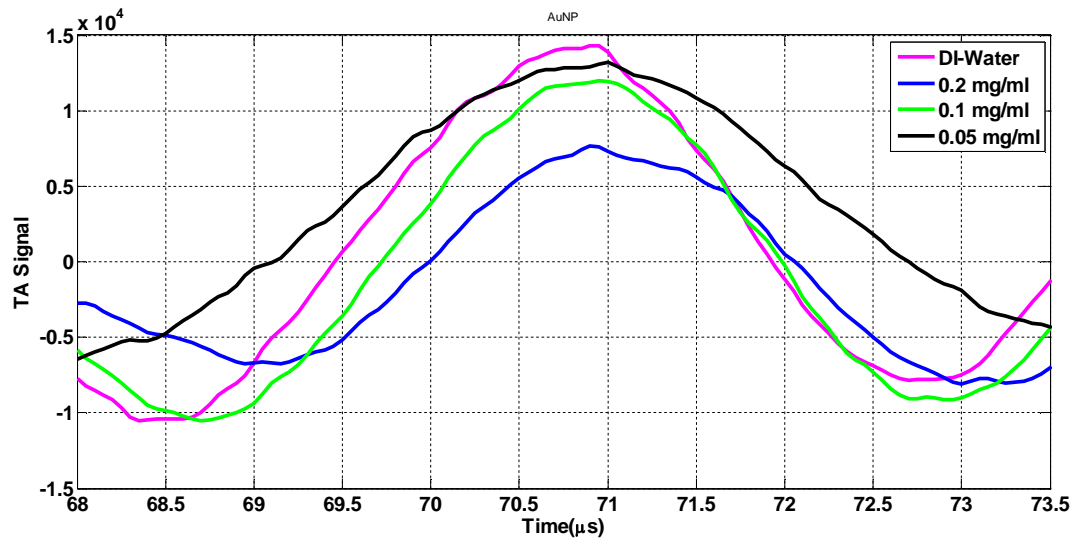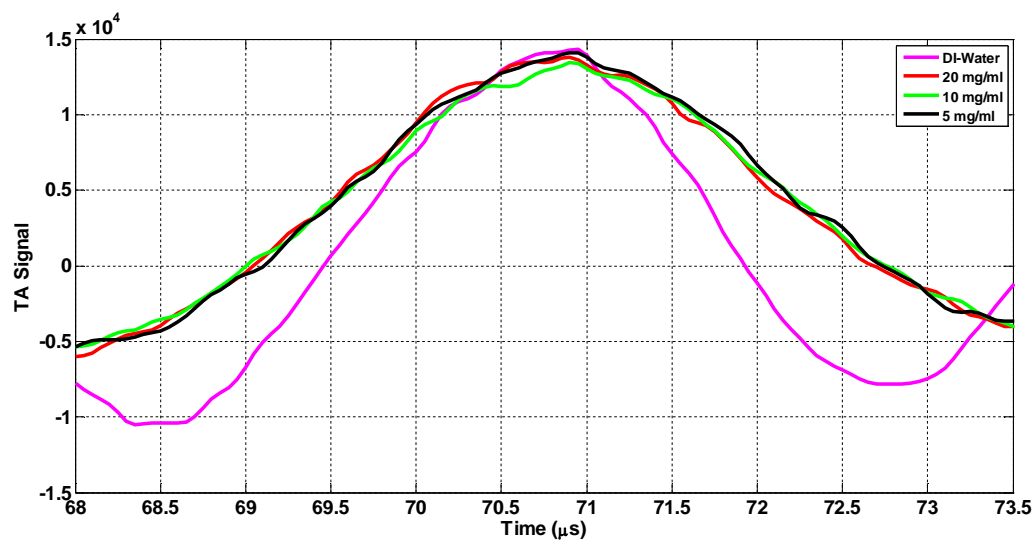
Fig. 37 Time resolved thermoacoustic signal of AuNCs.
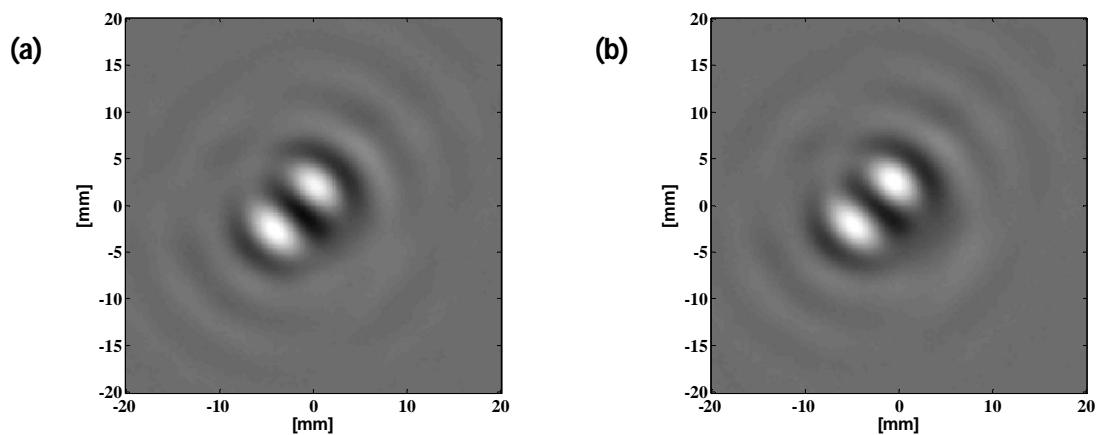
Fig. 38 TAT images of AuNCs. (a) 20 mg/ml AuNCs. (b) 10 mg/ml AuNCs. (c) 5 mg/ml AuNCs.
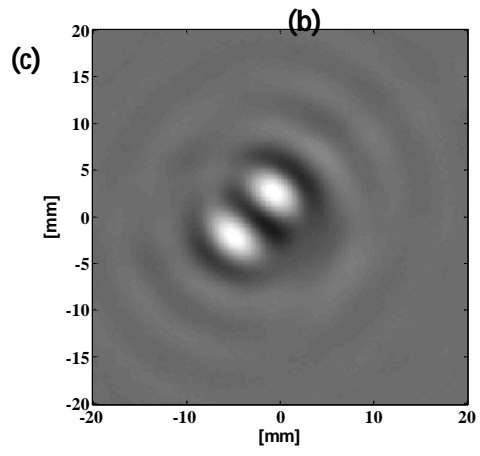
Fig. 38 Continued.

CHAPTER IV

AUNPs COMPUTATIONAL TEST OF MICROWAVE HEATING

4.1 Microwave Temperature Profile of DI-Water

As mentioned in 1.1 there is no consistent data about microwave (and RF) absorption properties of AuNPs. A report has shown that even low concentrations of AuNPs are able to generate heat up to two folds more than DI-water [12] while, Kim et al has investigated that AuNPs don't produce heat in microwave (and RF) region. In this area, a simple Mie simulation can provide critical insight and help to clarify this issue. Using Debye equations, water absorption can be calculated:

$$\mu_{abs} = \frac{2\pi f}{c10^{-7}} \left[\frac{\left(\sqrt{e_h'^2 + e_h''^2}\right) - e_h'}{2} \right]^{\frac{1}{2}} \tag{9}$$

Where e' and e'' are real and imaginary parts of dielectric function of water from Debye equations:

$$e_h' = e_{0v} + \frac{e_{0d} - e_{0v}}{1 + \omega^2 \tau^2}$$

$$e_h'' = \frac{\omega \tau (e_{0d} - e_{0v})}{1 + \omega^2 \tau^2} \tag{10}$$

In Eq. (10), $e_{0v} = 5.27, e_{0d} = 77.5,$ and $\tau = 0.8 \times 10^{-11}$ seconds [38]. Multiplying the water absorption to the cross-sectional area of the cuvette, and the power of the system, we end up with the power absorption of water:

$$P = W \times (1 - e^{-abs \times l}) \tag{11}$$

In Eq. (11), W is the irradiance of the system, which in our system has been set up at 30 W. abs. represents the water absorption at specific frequency, and l represents the

length of cuvette. By combining the power absorption of water, water capacity, and water mass (which varies with temperature and reaches maxima at 4° C) we derive the water heating. The heating rate of DI-water during two minutes is shown in Fig. 39.

$$Q = \frac{P}{m \times C_p}$$ (12)

4.2 Microwave Temperature Profile of AuNPs

As mentioned earlier, when a small size of AuNP is irradiated by light, the oscillating electric field causes the conduction electrons to oscillate coherently. When the electron cloud is displaced relative to the nuclei, a restoring force arises from Coulomb attraction between electrons and nuclei that results in oscillation of the electron cloud relative to the nuclear framework. The collective oscillation of the electrons is called the dipole plasmon resonance of the particle (sometimes denoted "dipole particle plasmon resonance" to distinguish from plasmon excitation that can occur in bulk metal or metal surfaces). Higher modes of plasmon excitation can occur, such as the quadrupole mode where half of the electron cloud moves parallel to the applied field and half moves antiparallel [49].

Using full Drude model, we can calculate the extinction coefficient of AuNPs in both dipole and quadrupole mode (Eq. (16) and Eq. (17), respectively):

$$\gamma = \gamma_{Bulk} + A\frac{V_F}{r}$$ (13)

$$e'_m = 1.53 - \frac{\omega_p^2}{\omega^2 + \gamma^2}$$ (14)

$$e''_m = \frac{\gamma \times \omega_p^2}{\omega^3 + \omega \gamma^2}$$ (15)

$$q_{Dipole} = \frac{18\pi V}{\lambda} e'^{\frac{1}{2}}_h \frac{e'_h e''_m - e'_m e''_h}{(e'_m + 2e'_h)^2 + (e''_m + 2e''_h)^2} \tag{16}$$

$$q_{Quadrupole} = \frac{16\pi^3}{\lambda^3} r^5 \frac{e'_h e''_m - e'_m e''_h}{e'^2_h + e''^2_h} \tag{17}$$

Very close thermal trend of DI-water recorded by CEM in our lab (plotted in dotted red in Fig. 39) to the simulated DI-water heating rate (plotted in blue in Fig. 39) validates the accuracy of this modeling. As the AuNPs were cleaned after synthesizing and resuspended into DI-water, the absorption of AuNPs solution includes DI-water absorption. So, AuNPs absorption is the summation of the total extinction coefficient of AuNPs in both dipole and quadrupole modes and DI-water absorption. Similar to power absorption of DI-water, the power absorption of AuNPs was calculated by multiplying the irradiance power by the system, cuvette area, and AuNPs absorption. The AuNPs heating computed by multiplying the AuNPs power absorption, water mass, and water capacity. Fig. 40 reveals the simulation of heating rate of AuNPs solution and AuNPs solution from experimental data recorded by CEM during one minute. Very similar temperature enhancement of these two, imply the validity of AuNPs heating rate simulation. Comparing simulated DI-water heating rate to the AuNPs temperature enhancement simulation indicates that AuNPs do not contribute in microwave heating.
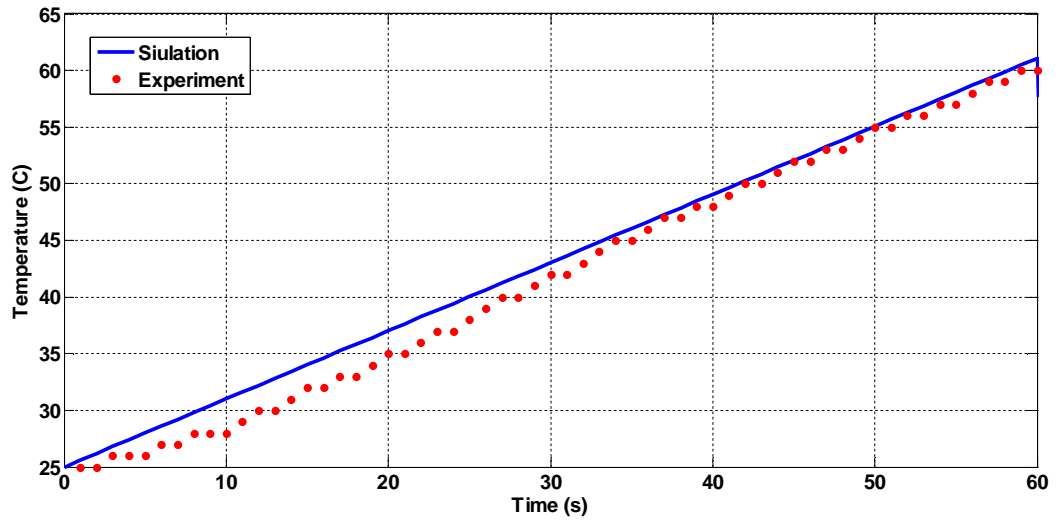
Fig. 39 Simulation of water temperature change.
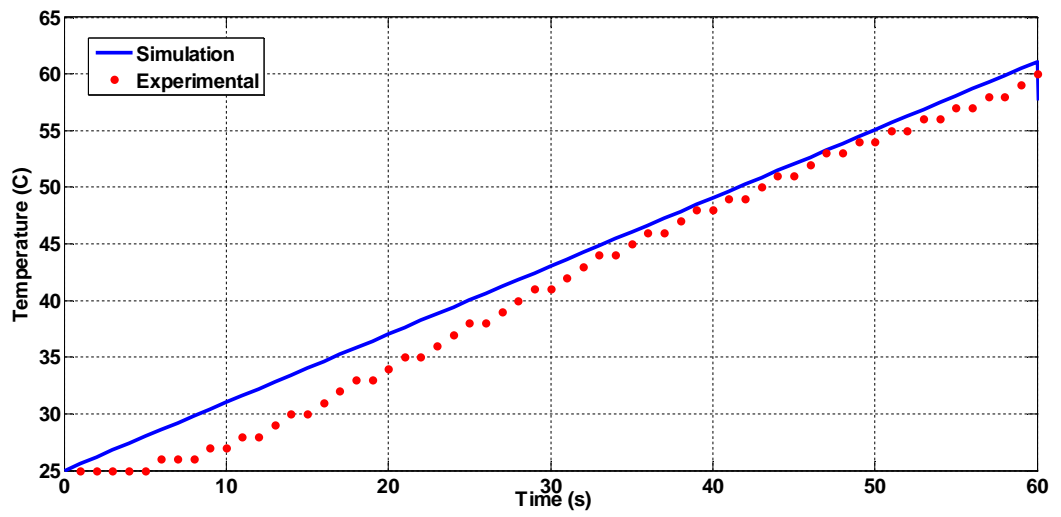
Fig. 40 Simulation of AuNPs solution temperature change.

CHAPTER V

CONCLUSION AND FUTURE WORK

In this research, we investigated the microwave properties of SPIONs, AuNPs and AuNCs for use as hyperthermic and contrast agents in a TAT system. In this experiment, the microwave properties of AuNCs were studied for the first time. The microwave behavior of aforementioned nanoparticles and DI-water were examined in three different steps. As DI-water is the main absorber in the biological samples, the trend of nanoparticles in absorbing microwave energy and transferring it into heat were compared with DI-water in each step.

First, different concentrations of nanoparticles were exposed to microwave energy at 3 GHz and the temperature enhancements of samples were recorded after one minute. The results shows that high concentrations of SPIONs are able to transfer microwave energy into heat and enhance the temperature up to 22° C compared to DI-water. Irradiating microwave energy to AuNPs, even at high concentrations, did not produce any significant temperature change compared to DI-water. In addition, microwave absorption of AuNPs was calculated using Mie theory. The simulation corroborates the negligible microwave absorption of AuNPs. AuNCs are capable of transferring microwave into heat at very high concentrations but still not as effectively as SPIONs. In the second step, the permittivity of nanoparticles was measured by a dip probe kit. Then, the microwave absorption spectrum of each sample was calculated by using permittivity data measurement. The results showed that by increasing SPIONs concentrations, the microwave absorption raised, while increasing AuNPs caused falling the microwave absorption down. This is due to smaller microwave absorption by smaller amount of DI-water in the AuNPs solution than that of only DI-water. Different concentrations of AuNCs solution absorb microwave energy less than DI-water but in contrast to AuNPs, the absorption ascended by increasing concentration. This different trend between AuNPs and AuNCs may arise from transition between sub-conduction bands in AuNCs

between 5d and 6sp. In the third and last step, nanoparticles were tested as contrast agents in a TAT system. As predicted from the results of first two steps, only SPIONs were able to improve TAT contrast compared to DI-water. All different concentrations of AuNCs provided the same contrast as DI-water, while AuNPs degraded the contrast of TAT image. In other words, the results in the first two steps were confirmed by in the last step.

In the future work, we suggest testing the applicability of using high concentration of SPIONs in biological samples. Also, the SPIONs and AuNCs can be examined as the hyperthermic agents for therapeutic purposes. In this research it was investigated that AuNCs have the potential to produce TAT contrast. However, further studies are still required in order to investigate the essential concentration of AuNCs to produce high TAT contrast.

REFERENCES

1. Picano, E., *Sustainability of medical imaging.* BMJ, 2004. **328**(7439): p. 578-580.

2. Ram, G., *Optimization of ionizing radiation usage in medical imaging by means of image enhancement techniques.* Medical Physics, 1982. **9**(5): p. 733-737.

3. Roobottom, C.A., Mitchell, G., Morgan-Hughes, G., *Radiation-reduction strategies in cardiac computed tomographic angiography.* Clin Radiol, 2010. **65**(11): p. 859-67.

4. Eustis, S., El-Sayed, M. A., *Why gold nanoparticles are more precious than pretty gold: Noble metal surface plasmon resonance and its enhancement of the radiative and nonradiative properties of nanocrystals of different shapes.* Chemical Society Reviews, 2006. **35**(3): p. 209-217.

5. Cai, W., Gao, T., Hong, H., and Sun, J.,, *Applications of gold nanoparticles in cancer nanotechnology.* Science and Apllications, 2008. **1**: p. 17-32.

6. Li, J.J., *Gold-Nanoparticle-Enhanced Cancer Photothermal Therapy.* Selected Topics in Quantum Electronics, IEEE Journal of, 2010. **16**(4): p. 989-996.

7. Nedyalkov, N.N., Imamova, S. E., Atanasov, P. A., Toshkova, R. A., and E.G. Gardeva, Yossifova, L. S., Alexandrov, M. T., Obara, M.,, *Interaction of gold nanoparticles with nanosecond laser pulses: Nanoparticle heating.* Applied Surface Science, 2011. **257**(12): p. 5456-5459.

8. Hanson, G.W., Monreal, R. C., Apell, S. P.,, *Electromagnetic absorption mechanisms in metal nanospheres: Bulk and surface effects in radiofrequency-terahertz heating of nanoparticles.* Journal of Applied Physics, 2011. **109**(12): p. 124306-124306-6.

9. Jin, X., Keho, A., Meissner, K., Wang, L. V., , *Iron oxide nanoparticles as a contrast agent in thermoacoustic tomography.* Proc. of SPIE, 2007. **6437**: p. 67370E.

10. Kim, D.K., Amin, M. S., Elborai, SH., Lee, S., Koseoglu, Y., Zahn, M., Muhammed, M.,, *Energy absorption of superparamagnetic iron oxide nanoparticles by microwave irradiation.* Journal of Applied Physics, 2005. **97**(10): p. 10J510-3.

11. Nie, L., Ou, Z., Yang, S., Xing, D.,, *Thermoacoustic molecular tomography with magnetic nanoparticle contrast agents for targeted tumor detection.* Med Phys, 2010. **37**(8): p. 4193-200.

12. Moran, C.H., Wainerdi, S. M., Cherukuri, T. K., Kittrell, C., Wiley, B. J., Nicholas, N. W., Curley, S. A., Kanzius, J. S., Cherukuri, P *Size-dependent joule heating of gold nanoparticles using capacitively coupled radiofrequency fields.* Nano research, 2009. **2**(5): p. 400.

13. Li, D., Jung, Y. S., Tan, S., Kim, H. K., Chory, E., Geller, D. A.,, *Negligible absorption of radiofrequency radiation by colloidal gold nanoparticles.* J Colloid Interface Sci, 2011. **358**(1): p. 47-53.

14. Ku, G., and Wang, L.V, *Scanning thermoacoustic tomography in biological tissue.* Med. Phys, 2000. **27.5**: p. 1195-1202.

15. Wang, Q. and J. Liu, *Nanoparticles Enhanced Hyperthermia*, in *Intracellular Delivery*, A. Prokop, Editor. 2011, Springer Netherlands. p. 567-598.

16. Mehdaoui, B., et al., *Optimal Size of Nanoparticles for Magnetic Hyperthermia: A Combined Theoretical and Experimental Study.* Advanced Functional Materials, 2011. **21**(23): p. 4573-4581.

17. Cherukuri, P., E.S. Glazer, and S.A. Curley, *Targeted hyperthermia using metal nanoparticles.* Advanced Drug Delivery Reviews, 2010. **62**(3): p. 339-345.

18. Gerweck, L.E., *Hyperthermia in Cancer Therapy: The Biological Basis and Unresolved Questions.* Cancer Research, 1985. **45**(8): p. 3408-3414.

19. Urano, M., *Response of a spontaneous murine tumor to hyperthermia: Factors which modify the thermal response in vivo.* Radiation Research, 1980. **83**(2): p. 312.

20. Gilchrist, R.K., Shorey, W. D., Hanselman, R. C., Depeyster, F. A., Yang, J., Medal, R., *Effects of Electromagnetic Heating on Internal Viscera: A Preliminary to the Treatment of Human Tumors.* Ann Surg, 1965. **161**: p. 890-6.

21. Ramanujan, R.V.a.L., L.L.,, *magnetic particles for hyperthermia treatment of cancer.* Proc. First Intl. Bioengg. Conf.,, 2004: p. 69-72.

22. Cheung, A.Y., *Microwave and radiofrequency techniques for clinical hyperthermia.* The British journal of cancer. Supplement, 1982. **5**: p. 16-24.

23. Wang, L.V., Hu, S., *Photoacoustic tomography: in vivo imaging from organelles to organs.* Science, 2012. **335**(6075): p. 1458-62.

24. Jie, C. and Y. Yang, *Quantitative photo-acoustic tomography with partial data.* Inverse Problems, 2012. **28**(11): p. 115014.

25. Li, W., Brown, P. K., Wang, L. V., Xia, Y., *Gold nanocages as contrast agents for photoacoustic imaging.* Contrast Media Mol Imaging, 2011. **6**(5): p. 370-7.

26. Bulte, J.W.M., *The chemistry of contrast agents in medical magnetic resonance imaging. edited by A. E. Merbach and E. Toth. Wiley, Chichester, 2001, £135*, in *NMR in Biomedicine* 2004, John Wiley & Sons, Ltd. p. 210-210.

27. Lou, C., et al., *Ultrashort Microwave-Induced Thermoacoustic Imaging: A Breakthrough in Excitation Efficiency and Spatial Resolution.* Physical Review Letters, 2012. **109**(21): p. 218101.

28. Goodarzi, A., Sahoo, Y., Swihart, M.T., and Prasad, P.N, *Aqueous ferrofluid of citric acid coated magnetic nanoparticles.* Mat. Res. Soc. Symp. Proc, 2004. **789**: p. N6.6.1-N6.6.6.

29. Xu, M., et al., *Breast cancer imaging by microwave-induced thermoacoustic tomography.* 2005: p. 45-48.

30. Justin, T., *Thermoacoustic tomography in elastic media.* Inverse Problems, 2012. **28**(5): p. 055004.

31. Ke, H., Erpelding, T. N., Jankovic, L., Liu, C., Wang, L. V.,, *Performance characterization of an integrated ultrasound, photoacoustic, and thermoacoustic imaging system.* J Biomed Opt, 2012. **17**(5): p. 056010.

32. Xu, M. and X. Minghua, *Time-domain reconstruction algorithms and numerical simulations for thermoacoustic tomography in various geometries.* IEEE Transactions on Biomedical Engineering, 2003. **50**(9): p. 1086.

33. Kruger, R.A., Miller, K. D., Reynolds, H. E., Kiser, W. L., Reinecke, D. R., Kruger, G. A.,, *Breast cancer in vivo: contrast enhancement with thermoacoustic CT at 434 MHz-feasibility study.* Radiology, 2000. **216**(1): p. 279-283.

34. Ku, G., Fornage, B. D., Jin, X., Xu,M., Hunt, K. K., Wang, L.V, *Thermoacoustic and photoacoustic tomography of thick biological tissues toward breast imaging.* Technology in Cancer Research & Treatment, 2005. **4**: p. 559-565.

35. Yuan, X., Wang, L. V., *Effects of acoustic heterogeneity in breast thermoacoustic tomography.* Ultrasonics, Ferroelectrics and Frequency Control, IEEE Transactions on, 2003. **50**(9): p. 1134-1146.

36. Burgholzer, P., Hofer, C., Paltauf, G., and S. Haltmeier., O.,, *Thermoacoustic tomography with integrating area and line detectors.* IEEE Trans Ultrason Ferroelectr Freq Control, 2005. **52**(9): p. 1577-1583.

37. Kruger, R.A., Kiser, W. L., Reinecke, D. R., Kruger, G. A., Miller, K. D.,, *Thermoacoustic molecular imaging of small animals.* Mol Imaging, 2003. **2**(2): p. 113-23.

38. Yuan, X., Minghua, X., Wang, L. V.,, *Exact frequency-domain reconstruction for thermoacoustic tomography. II. Cylindrical geometry.* Medical Imaging, IEEE Transactions on, 2002. **21**(7): p. 829-833.

39. Minghua, X., Wang, L. V., *Time-domain reconstruction for thermoacoustic tomography in a spherical geometry.* Medical Imaging, IEEE Transactions on, 2002. **21**(7): p. 814-822.

40. Xu, Y., Feng, D., and Wang, L.V, *Exact frequency-domain reconctruction for thermoacoustic tomography- planer geometry.* IEEE TRANSACTIONS ON MEDICAL IMAGING. **21**: p. 823-828.

41. Jeong, U., Teng, X., Wang, Y,. Yang, H., Xia, Y.,, *Superparamagnetic Colloids: Controlled Synthesis and Niche Applications.* Advanced Materials, 2007. **19**(1): p. 33-60.

42. Batlle, X., and A, Labarta., , *Finit-size effect in fine particles magnetic and transport properties.* J. Phys. D: Apply. Phys, 2002. **35**: p. R15-R42.

43. Denizot, B., Tanguy, G., Hindre, F., Rump, E., Lejeune, J., and Jallet, P, *The prepration of magnetic nanoparticles for biomedical.* J.Collid interface Sci. , 2001. **209**: p. 66-71.

44. Hafeli, U., Schutt, W., Teller, J. and Zborowski, M, *Scientificand Clinical Applications of Magnetic Carriers*, 1997, New York: Plenum.

45. Philipse, A.P., van Bruggen, M., Pathmamanoharan, C.,, *Magnetic silica dispersions: preparation and stability of surface-modified silica particles with a magnetic core.* Langmuir, 1994. **10**(1): p. 92-99.

46.   Jordan, A., *Presentation of a new magnetic field therapy system for the treatment of human solid tumors with magnetic fluid hyperthermia.* Journal of magnetism and magnetic materials, 2001. **225**(1-2): p. 118.

47.   Daniel, M.-C. and D. Astruc, *Gold Nanoparticles: Assembly, Supramolecular Chemistry, Quantum-Size-Related Properties, and Applications toward Biology, Catalysis, and Nanotechnology.* Chemical Reviews, 2003. **104**(1): p. 293-346.

48.   El-Sayed. M. A., *Some Interesting Properties of Metals Confined in Time and Nanometer Space of Different Shapes.* Accounts of Chemical Research, 2001. **34**(4): p. 257-264.

49.   Kelly, K.l., Coronado, E., Zhao, L., Schatz, G. C., *The Optical Properties of Metal Nanoparticles: The Influence of Size, Shape, and Dielectric Environment.* The Journal of Physical Chemistry B, 2002. **107**(3): p. 668-677.

50.   Honda, M., Saito, Y.,Smith, Nicholas I., Fujita, K., Kawata, S.,, *Nanoscale heating of laser irradiated single gold nanoparticles in liquid.* Opt. Express, 2011. **19**(13): p. 12375-12383.

51.   Huang, X., Jain, P. K., El-Sayed, I. H., El-Sayed, M. A., *Gold nanoparticles: interesting optical properties and recent applications in cancer diagnostics and therapy.* Nanomedicine, 2007. **2**(5): p. 681-93.

52.   He, Y.Q., Liu, S. P., Kong, L.,Liu, Z. F.,, *A study on the sizes and concentrations of gold nanoparticles by spectra of absorption, resonance Rayleigh scattering and resonance non-linear scattering.* Spectrochim Acta A Mol Biomol Spectrosc, 2005. **61**(13-14): p. 2861-6.

53.   Cardinal, J., *Noninvasive radiofrequency ablation of cancer targeted by gold nanoparticles.* Surgery, 2008. **144**(2): p. 125.

54.   Jain, P.K., Lee, K. S., El-Sayed, I. H., El-Sayed, M A.,, *Calculated Absorption and Scattering Properties of Gold Nanoparticles of Different Size, Shape, and*

Composition: Applications in Biological Imaging and Biomedicine. The Journal of Physical Chemistry B, 2006. **110**(14): p. 7238-7248.

55. Gannon, C.J., Patra, C. R., Bhattacharya, R., Mukherjee, P., Curley, S. A., *Intracellular gold nanoparticles enhance non-invasive radiofrequency thermal destruction of human gastrointestinal cancer cells.* J Nanobiotechnology, 2008. **6**: p. 2.

56. Xavier, P.L., Chaudhari, K., and A. Baksi, Pradeep, T.,, *Protein-protected luminescent noble metal quantum clusters: an emerging trend in atomic cluster nanoscience.* Nano Rev, 2012. **3**(10): p. 3.

57. Hardman, R., *A Toxicologic Review of Quantum Dots: Toxicity Depends on Physicochemical and Environmental Factors.* Environ Health Perspect, 2006. **114**(2).

58. Lin, C.J., Lee, C, Hsieh, J., Wang, H., Li, J.K., Shen, J., Chan, W., Yeh, H., Chang, W.H., *Synthesis of fluorescent metallic nanoclusters toward biomedical applications recent progress* J. of Medical and Biological Engineering, 2009. **29(6)**: p. 276-283.

59. Jin, R., *Quantum sized, thiolate-protected gold nanoclusters.* Nanoscale, 2010. **2**(3): p. 343-362.

60. Qian, H., Zhu, M., Wu, Z., Jin, R., *Quantum sized gold nanoclusters with atomic precision.* Acc Chem Res, 2012. **45**(9): p. 1470-9.

61. Link, S., El-Sayed, M. A., *Optical properties and ultrafast dynamics of metallic nanocrystals.* Annu Rev Phys Chem, 2003. **54**: p. 331-66.

62. Lin, C.J.Y., T., Lee, C., and S.H. Huang, Sperling, R A., Zanella, M., Li, J K.,Shen, J., Wang, H., Yeh, H., Parak, W. J., Chang, W H.,, *Synthesis, Characterization, and Bioconjugation of Fluorescent Gold Nanoclusters toward Biological Labeling Applications.* ACS Nano, 2009. **3**(2): p. 395-401.

63.   Akola, J., Walter, M., Whetten, R. L., Häkkinen, H., Grönbeck, .,, *On the Structure of Thiolate-Protected Au25.* Journal of the American Chemical Society, 2008. **130**(12): p. 3756-3757.

64.   Zhu, M., Aikens, C. M., Hollander, F. J., Schatz, G C., Jin, R.,, *Correlating the Crystal Structure of A Thiol-Protected Au25 Cluster and Optical Properties.* Journal of the American Chemical Society, 2008. **130**(18): p. 5883-5885.

65.   Link, S., Beeby, A., FitzGerald, S., El-Sayed, M A., Schaaff, T. G., Whetten, R L.,, *Visible to Infrared Luminescence from a 28-Atom Gold Cluster.* The Journal of Physical Chemistry B, 2002. **106**(13): p. 3410-3415.

66.   Bigioni, T.P., Whetten, R. L., Dag, Ö.,, *Near-Infrared Luminescence from Small Gold Nanocrystals.* The Journal of Physical Chemistry B, 2000. **104**(30): p. 6983-6986.

67.   Huang, T., Murray, R. W.,, *Visible Luminescence of Water-Soluble Monolayer-Protected Gold Clusters.* The Journal of Physical Chemistry B, 2001. **105**(50): p. 12498-12502.

68.   Wilcoxon, J.P., Martin, J. E., Parsapour, F., Wiedenman, B., Kelley, D. F.,, *Photoluminescence from nanosize gold clusters.* The Journal of Chemical Physics, 1998. **108**(21): p. 9137-9143.

69.   Sakanaga, I., Inada, M.,, T. Saitoh, Kawasaki, H., Iwasaki, Y.,, and T. Yamada, Umezu, I., Sugimura, A.,, *Photoluminescence from Excited Energy Bands in Au_25 Nanoclusters.* Applied Physics Express, 2011. **4**(9): p. 095001.

70.   Dozier, D., Palchoudhury, S., and Bao, Y .,, *Synthesis of iron oxide nanoparticles with biological coating.* J. Science and Health at The University of Alabama, 2010. **7**: p. 16-18.

71.   Goodarzi, A., Sahoo, Y., Swihart, M.T.,Prasad, P.N, *Aqueous ferrofluid of citric acid coated magnetic nanoparticles.* Mat. Res. Soc. Symp. Proc., 2004. **789**: p. N6.6.1-N6.6.6.

72.   Jamison, J., Bryant, E.,.,Kadali, S., Wong, M., Colvin, V., Matthews, K., Calabretta, M.,, *Altering protein surface charge with chemical modification modulates protein–gold nanoparticle aggregation.* Journal of Nanoparticle Research, 2011. **13**(2): p. 625-636.

73.   Shang, L., Azadfar, N., and F. Stockmar, Send, W., Trouillet, V., Bruns, M., Gerthsen, D., Nienhaus, G. U.,, *One-pot synthesis of near-infrared fluorescent gold clusters for cellular fluorescence lifetime imaging.* Small, 2011. **7**(18): p. 2614-20.

74.   Acosta, S., et al., *On the multi-frequency inverse source problem in heterogeneous media.* Inverse Problems, 2012. **28**(7): p. 075013.

75.   Leadbeater. N., M.C., <*Clean, fast organic chemistry: Microwave- assited laboratory experiment.pdf*>. 2006: p. 8.

76.   Kostli, K.P., Frenz, M., Bebie, H., Weber, H. P.,, *Temporal backward projection of optoacoustic pressure transients using fourier transform methods.* Phys Med Biol, 2001. **46**(7): p. 1863-72.

APPENDIX

```matlab
%Metal NPs:  Model Extinction at Microwave Frequencies
%dipole + quandrapole modes (a1 + b1) - does not include the x^5 a1
term
%as the b1 term can become large if abs(epsilonm/epsilonh)>>1

%water modeled with Debye model from B&H p264 - microwave model


clear all;

%Physical constants
c = 3*10^(17);  %Speed of light (nm/s)
epsilon0 = 8.85*10^(-12); %permittivity of free space

%material properties Au
tb = 25*10^(-15); %Scattering time in bulk material (s)
gammab = 1/tb; %bulk damping term (1/s)
lp = 145; %plasma wavelength (nm)from Etchegoin 2006
wp = 2*pi*c/lp; %plasma frequency (rad/s)
%wp = 1.37*10^16; %plasma frequency (rad/s)

%material properies Water
t = 0.8*10^(-11); %taken from B&H p264
e0d = 77.5;
e0v = 5.27;

%experimental conditions
nh = 70^(1/2); %host index of refraction
eh = nh^2; %host dielectric function



%Drude Model coefficients
vF = 1.4*10^15; %Fermi velocity of electrons in Au (nm/s)
A = 3/4; %from Kreibig
rad = [5 10 20 50 100 150 250]; %particle size
m = size(rad,2);

%Frequency loop
fmin = 1*10^7; %initial frequency (Hz)
fmax = 1*10^11; %final frequency (Hz)
fstep = fmin;
n = ((fmax-fmin)/fstep) +1; %total number of frequency steps


%initialize arrays
ext = zeros(n,m); %extinction dipole
extquad = zeros(n,m); %extinction quadrapole
```

```matlab
freq = zeros(n,1);
emp = zeros(n,m);
empp = zeros(n,m);
gamma = zeros(m,1);
sigma = zeros(n,m); %conductivity
Heating_Ratio = zeros(n,m); %global heating ratio normalized by 5 nm NP

cntsize = 0;
cntf = 0; %start counter

for cntsize = 1:m
    %cntsize = cntsize + 1;
    %rad(cntsize) = r;
    r = rad(1,cntsize);
    gamma(cntsize) = gammab + (A*vF/r);

    for F = fmin:fstep:fmax %step frequency
        cntf = cntf+1;
        freq(cntf)=F;
        w = 2*pi*F; %angular frequency

        % Water permittivity/abs
        ehp(cntf) = e0v + (e0d - e0v)/(1 + (w^2)*(t^2));
        ehpp(cntf) = (w*t*(e0d - e0v))/(1 + (w^2)*(t^2));
        waterabs(cntf) = (2*pi*F/(c*10^(-7)))*(((ehp(cntf)^2 +
ehpp(cntf)^2)^(0.5) - ehp(cntf))/2)^(0.5); %calc in 1/cm

        %Full Drude Model
        emp(cntf,cntsize) = 1.53 - ((wp^2)./(w^2 + gamma(cntsize).^2));
%real part of dielectric function
        empp(cntf,cntsize) = (wp^2).*(gamma(cntsize))./(w*(w^2 +
gamma(cntsize).^2)); %imaginary part of dielectric function
        sigma(cntf,cntsize) = epsilon0*w*empp(cntf,cntsize);

        extdipole(cntf,cntsize) =
(18*pi)*((4/3)*pi*r^3)*(F/c)*(ehp(cntf)^(1/2))*(ehp(cntf)*empp(cntf,cnt
size) -
emp(cntf,cntsize)*ehpp(cntf))/((emp(cntf,cntsize)+2*ehp(cntf))^2+(empp(
cntf,cntsize)+2*ehpp(cntf))^2); %extinction coefficient
        extquad(cntf,cntsize) =
(16/15)*pi^4*(F/c)^3*r^5*(ehp(cntf)*empp(cntf,cntsize) -
emp(cntf,cntsize)*ehpp(cntf))/(ehp(cntf)^2 + ehpp(cntf)^2);
        ext(cntf,cntsize) = extdipole(cntf,cntsize) +
extquad(cntf,cntsize);
        eff(cntf,cntsize) = ext(cntf,cntsize)/(pi*r^2);


    end

    cntf = 0;
end
```

```matlab
for cntsize = 1:m
    for cntf = 1:n
        Heating_Ratio(cntf,cntsize) =
(5/rad(cntsize))^3*ext(cntf,cntsize)/ext(cntf,1);
    end
end


color = ['b' 'g' 'r' 'c' 'm' 'y' 'k'];


figure;
for i = 1:1:m
    loglog(freq,ext(:,i),color(i));
    hold on;
end
title('Extinction Cross Section (nm^2)');
legend('5','10','20','50','100','150','250');


figure;
for i = 1:1:m
    semilogx(freq,sigma(:,i),color(i));
    hold on;
end
title('Conductivity');
legend('5','10','20','50','100','150','250');


figure;
loglog(freq,waterabs);
title('Water Absorption (1/cm)');
xlabel('frequency (Hz)');


%Water heating - our system - cuvette is dia = 15mm, h = 8.9cm
abs = waterabs(300); %use 2.45 GHz
time = (1:1:121)'; %over 120 s
waterCp = 4187; %water heat capacity in J/(kg K)
watermass = .0157; %15ml cuvette in kg
cuvettearea = 1; %crossectional area of cuvette in cm2
cuvettelength = 2.36; %length of cuvette in cm - circumference at half
the radius
irradiance = 30; %in W 30W through the beaker
powerabs = irradiance*(1-exp(-abs*cuvettelength));
temp = zeros(121,1);
temp(1) = 25; %start at room temp
for i = 1:120
    dtemp=powerabs*1/watermass/waterCp; %change in temp
    temp(i+1)=temp(i)+dtemp;
end
figure;
```

```matlab
plot(time-1,temp)
title('Water Heating - Meissner Lab');
xlabel('time (s)');
ylabel('Temperature (C)');


%NP/Water heating - our system - cuvette is dia = 15mm, h = 8.9cm
abs = waterabs(300)+ 1e-9/10^3*6.02e23*ext(245,1)/1e14; %use 2.45 GHz
time = (1:1:121)'; %over 120 s
waterCp = 4187; %water heat capacity in J/(kg K)
watermass = .0157; %15ml cuvette in kg
cuvettearea = 1; %crossectional area of cuvette in cm2
cuvettelength = 2.36; %length of cuvette in cm - circumference at half
the radius
irradiance = 30; %in W 30W through the beaker
powerabs = irradiance*(1-exp(-abs*cuvettelength));
temp = zeros(121,1);
temp(1) = 25; %start at room temp
for i = 1:120
    dtemp=powerabs*1/watermass/waterCp; %change in temp
    temp(i+1)=temp(i)+dtemp;
end
figure;
plot(time-1,temp)
title('NP/Water Heating - Meissner Lab');
xlabel('time (s)');
ylabel('Temperature (C)');
```